Chemistry & Physics of Complex Systems Facility

The Chemistry & Physics of Complex Systems (CPCS) Facility supports the U.S. Department of Energy (DOE) mission of fostering fundamental research in the natural sciences to provide the basis for new and improved energy technologies and for understanding and mitigating the environmental impacts of energy use and contaminant releases. This research provides a foundation for understanding interactions of atoms, molecules, and ions with materials and with photons and electrons. Particular emphasis is on interfacial processes.

A distinguishing feature of research at national laboratories is their approach to problem-solving. Significant scientific issues are addressed using focused and multidisciplinary investigative teams with each team member bringing a particular skill and capability to bear on the problem. This approach accelerates progress. The same approach—involving groups of scientists within the program as well as collaborators from throughout Pacific Northwest National Laboratory (PNNL) and the external scientific community—is inherent in how the CPCS Facility is managed.

The CPCS Facility and its staff have particular capabilities and expertise that support user research involving preparation and spectroscopic analysis of molecular clusters; high-resolution imaging of biological samples and studies of cellular processes, including DNA damage and repair and low-dose radiation processes; ultra-fast and non-linear optical spectroscopies; ultra-high-resolution spectroscopy for measurements of electronic and geometric structures and dynamics; surface and interface structure, chemical reaction dynamics and kinetics; ion-molecule traps and storage technology; and specialized chambers, instruments, and models for chemical reactivity and analysis of atmospheric species including aerosols.

Our research underpins the fundamental understanding of chemical transport and reactivity in the condensed phase. It addresses the underlying uncertainties in thermal and non-thermal (i.e., radiation) chemistry, interfacial molecular and ionic transport, and other processes in complex natural and human-made systems related to energy use, environmental remediation, waste management, and understanding biological responses to environmental stresses. One focus is on structures and processes of molecular and nanoscale systems in complex environments such as condensed phases and interfaces. Research guides the development of new materials and approaches for clean and efficient energy use.

> **Instrumentation & Capabilities**
> - Reaction mechanisms at solid, liquid, and gas interfaces
> - High-energy processes at environmental interfaces
> - Cluster models of the condensed phase
> - Single-molecule spectroscopy and biomolecular sciences
> - Ultra-sensitive and environmental analysis

Another central feature is the development of innovative experimental methods with broad applications to research in the natural sciences. In addition to this core research, the CPCS group has expanded its interests into two major new areas: 1) detecting and monitoring trace atmospheric species, including gaseous and particulate matter, and 2) studying biological processes important in the environment and health, including live cell imaging to observe the reaction dynamics of functioning biological systems in realtime, single-molecule spectroscopy to understand protein-protein interactions and DNA damage and repair, and novel instrumentation for studying cellular responses to low-dose radiation.

The capabilities of the CPCS Facility support research in the following five areas.

Reaction Mechanisms at Solid, Liquid, and Gas Interfaces. Research in this area focuses on developing fundamental molecular information about processes occurring at the interfaces between environmentally important liquids, solids, and gases. For example, a common element in environmental restoration is the need to understand molecular processes 1) in aqueous solutions and at the interface between aqueous and organic solutions, and 2) at the interface between aqueous solutions and environmentally important solid materials. Examples of instruments that enable this research are shown in Figures 1 and 2.

Molecular processes occurring at liquid-liquid interfaces also play an important role in the subsurface transport of contaminants such as organic solvents (e.g., chlorinated hydrocarbons) released into soil and groundwater. Processes at the gas-liquid interface are critical in atmospheric transport processes.

Figure 1. State-of-the-art molecular beam-surface scattering and kinetics instrument.

Figure 2. This combined instrument allows fluorescent optical microscopes and magnetic resonance microscopes to focus on the same samples at the same time.

Model systems such as amorphous solid water permit detailed studies of solvation and the effects of solvation on chemical reactivity. These studies provide information about intermolecular interactions that lay the foundation for accurate modeling of solution processes. Studies provide information about factors controlling the rates of reactions in
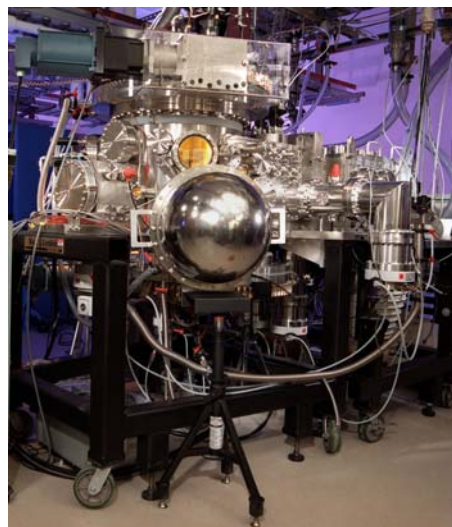
solution essential to both predicting the fate of contaminants in aqueous environments and influencing the selectivity of ligands for specific ions important in developing separations agents for waste treatment.

It is also crucial to understand molecular processes at the interface between aqueous solutions and environmentally important materials, such as aerosol particles, minerals, and glasses. This addresses fundamental science questions about contaminant fate and transport and waste immobilization. Because most environmental materials are in an oxidized form, we emphasize the structure and chemistry of oxide materials, especially naturally occurring oxides of silicon, aluminum, and iron. The adsorption of species on and their incorporation in soil

Figure 3. Laser desorption experiments to investigate the effects of electronic excitation on crystalline materials.

minerals affect their transport through soil. Mineral interfaces can enhance or retard reactivity as well as transform contaminants. Knowledge of molecular processes at solid-liquid interfaces is also important to understand the stability of glasses proposed for encapsulating high-level radioactive waste. Over the long half-lives of radionuclides, water can degrade these waste-encapsulating glasses resulting in higher-than-expected releases of radionuclides.

High-Energy Processes at Environmental Interfaces. Research in this area focuses on obtaining a mechanistic understanding of chemical transformations resulting from electronic excitation in condensed-phase materials relevant to the DOE environmental cleanup mission. Energetic processes are important in the degradation of mixed wastes due to radiolytic decay-driven chemistry that occurs in the solid and liquid phases of stored radioactive waste and in final waste storage forms. Examples of capabilities that enable this research are shown in Figures 3 and 4.
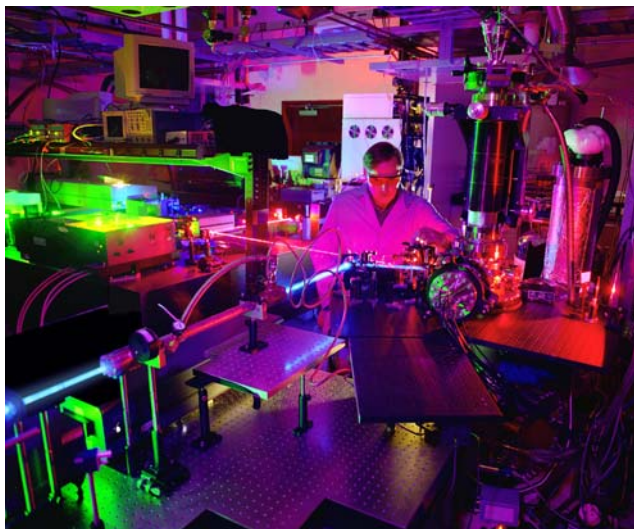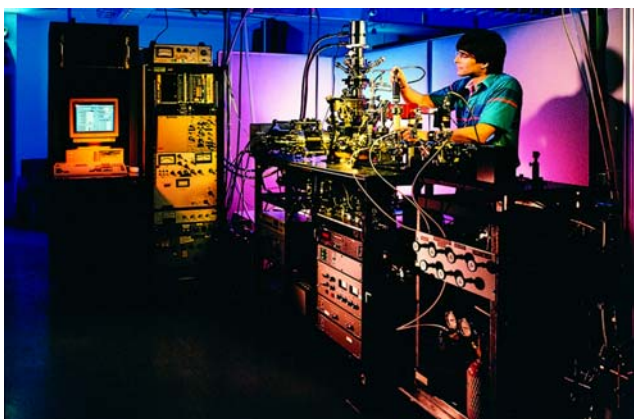

Figure 4. Electron-stimulated surface reaction apparatus is used to study non-thermal reactions that occur on surfaces or at interfaces.

Reactions occurring at interfaces are of particular interest for characterizing material composition and response to electronic excitation. We use pulsed femtosecond and nanosecond laser sources to study laser-solid interactions in a combined experimental and theoretical program. Our goal is to develop models for excited state reactions by measuring ultra-fast dynamic processes and by demonstrating laser control of solid-state chemistry.

Cluster Models of the Condensed Phase. This research is aimed at providing a molecular-level understanding of solvation and subsequent reactions in simple and complex systems as they relate to the chemistry of complex wastes, contaminated solids and groundwater, and other systems found in nature. A major experimental and theoretical effort is devoted to understanding surface and interface properties using cluster models to study structure and bonding. Small and controllable cluster systems provide atomic-level models that enable us to understand bulk surfaces and defect sites. They are also an excellent testing ground to benchmark theories intended for large and "real-world" systems. A productive collaboration in this area is illustrated in Figure 5.
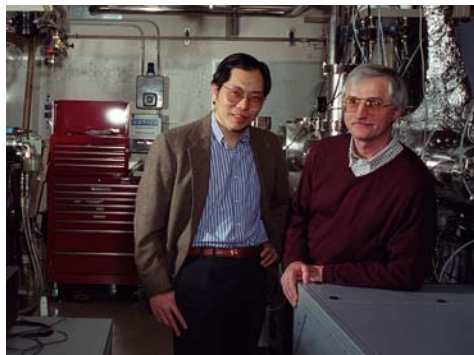

Figure 5. CPCS user/collaborators Lai-Sheng Wang, Washington State University, Richland, Washington, and Alex Boldyrev, Utah State University, Logan, Utah, are combining experimental and theoretical approaches to understand the unique properties and characteristics of metal clusters. Their research is at the forefront of cluster science.

Single-Molecule Spectroscopy and Biomolecular Sciences. This research emphasizes single-molecule spectroscopy and high-resolution biological imaging techniques for studying biological systems. Recent advances in fluorescence microscopy, at PNNL and elsewhere, make it possible to detect single molecules at room temperature and to conduct spectroscopic measurements to monitor their dynamic processes. We have demonstrated fluorescence imaging of single molecules by two-photon excitation with a femtosecond laser. This approach has several advantages—the excitation volume is small, the penetration is deep, and photo-damage is reduced for biological samples—thus offering the opportunity of viewing chemical reactions in a living cell in realtime. Structures are known for many proteins that perform vital cell functions, including DNA damage repair, reaction catalysis, and cell signaling. Nanoscale-structure materials will affect their properties; an example is shown in Figure 6. However, how they perform these functions is generally not known. Single-molecule and single-cell measurements provide real-time data on the molecular motions involved during these functions and how the timing of these
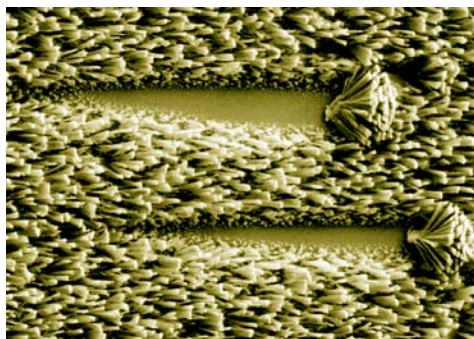

Figure 6. Nanostructures could be used to control and enhance chemical reactivity. CPCS researchers are trying to determine how molecules enter pores and are captured and eventually released.

reactions is correlated with other cellular biological activities. These data are likely to produce new information that is otherwise hidden, and will open up exciting possibilities for probing cellular processes.

Another research area is that of cellular response to low-dose radiation at levels below standard detection limits. A novel spatially resolved cell irradiator allows the selective irradiation of individual cells to reveal the individual pathways that lead to radio-adaptive responses. Information obtained from use of this instrument will enable researchers to understand the biological consequences and health effect associated with very low radiation doses. Such knowledge can help form more technically rigorous bases for human health and environmental protection standards.

Ultra-Sensitive and Environmental Analysis. Research in this area focuses on developing a suite of instrumentation for fast, accurate, highly sensitive, and discriminatory real-time analyses of chemical and biological natural or human-made agents. Such instruments are ideally suited for identifying and quantifying many gases and pollutants, trace isotopic species, metabolic products in the breath, and chemical precursors and products from industrial processes. Some of these techniques can be developed for remote probing over long optical paths for remote interrogation of trace absorption features. Our infrared methods are supported by a state-of-the-art, high-resolution infrared spectroscopy laboratory, shown in Figure 7,

Figure 7. The high-resolution infrared spectroscopy laboratory is used by numerous users and U.S. government agencies to obtain high-resolution infrared spectra for applications in remote sensing, atmospheric science, space and planetary research, and infrared databases.

that is also used for studies of the structures and dynamics of molecular species important in contaminant chemistry, photochemistry, and atmospheric processes.

Characterization of particulate matter in the atmosphere represents a unique challenge. Several approaches are employed that, in combination, are designed to understand the evolving inventory of atmospheric particulate matter and how particulates are changed by reactions with gas-phase species, photochemistry, and condensation and evaporation processes. One approach uses new mass spectrometric techniques for aerosol analysis. This instrumentation is built around a laser desorption/ionization mass spectrometer with an asymmetric ion trap for simultaneous positive/negative ion detection. It provides real-time sampling and analysis of aerosol particles in a field-deployable unit more compact and less costly than current instruments.

In conjunction with this instrumentation, new devices are being developed and deployed to collect and preserve field samples for future automated analysis of individual particles in the laboratory. These same samples enable the chemical reactivity characterization of native aerosols for comparison to laboratory studies of the formation and reactivity of model aerosol species. These studies are complemented by fundamental studies of the gas-phase chemistry of aerosol precursor molecules.

Laser Control of Product Electronic State: Desorption from Alkali Halides

KM Beck,[a] AG Joly,[b] NF Dupuis,[c] P Perozzo,[d] WP Hess,[a] PV Sushko,[e] and AL Shluger[e]

(a)   W.R. Wiley Environmental Molecular Sciences Laboratory, Richland, Washington
(b)   Pacific Northwest National Laboratory, Richland, Washington
(c)   University of California, Santa Barbara, California
(d)   Mary Baldwin College, Staunton, Virginia
(e)   University College London, United Kingdom

It has been demonstrated that surface-selective laser excitation and ultrasensitive atomic-desorption techniques can be used to study the behavior of electronically excited alkali halide surfaces (Hess et al. 2002; Joly et al. 2003). A sequence of photo-induced processes involving the excitation, self-trapping, and decomposition of surface excitons produces surface F centers (halogen vacancies that trap an electron) and desorbed hyperthermal halogen atoms. Further, the decomposition of the surface exciton leads to desorption of a mixture of ground- and spin-orbit excited halogen atoms.

Through our experimental and theoretical collaborative effort, we have determined that, if the values of the surface exciton energy and the halogen spin-orbit splitting are known, the halogen atom electronic state distribution and yield could be controlled using tunable laser excitation. For KCl, we found that, by tuning the excitation laser photon energy across the absorption threshold, the relative Cl* yield could be made to vary from near zero to 80%, thus dramatically confirming the exciton model and our laser control approach. A similarly large range also was obtained for NaCl. We achieved these results by determining and exploiting the shift between surface and bulk exciton bands and by using photon energies less than those necessary to produce significant bulk absorption or reaction.

Figure 1 is a schematic diagram of bulk and surface energy levels. Significantly, the spin-orbit splitting in alkali chlorides is small ($\Delta E \sim 0.1$ eV), so both the $\Gamma_{3/2}$ and $\Gamma_{1/2}$ exciton states are located within the lowest absorption feature at room temperature (Figure 1a). Furthermore, in comparison, the shift between the surface and bulk exciton is large (>0.5 eV). These two factors constitute the requirements for laser control over the halogen atom electronic state distribution.
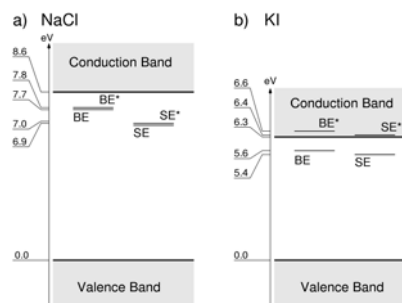

Figure 1. Schematic diagram of bulk electronic bands and bulk and surface exciton states for a) NaCl and b) KI. SE and SE* are surface exciton states with J = 3/2 and 1/2, respectively. BE and BE* are bulk exciton states.

The Cl and Cl* velocity profiles, from a NaCl (100) surface at room temperature irradiated at 7.5 eV, are shown in Figure 2 (top graph). To generate the velocity profile, the Cl-atom yield is plotted as a function of the delay between pump and probe lasers. The velocity profiles can then be converted to kinetic energy distributions by applying the appropriate Jacobian transform (Figure 2 [bottom graph]) (Beck et al. 2001).
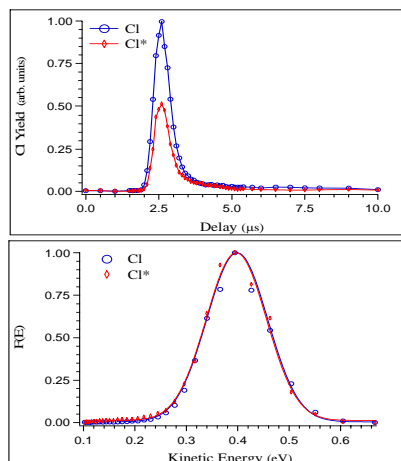
Figure 3 (left graph) displays relative spin-orbit yields measured for room temperature KCl, as a function of photon energy, and Figure 3 (right image) shows the available data for KI. One can clearly see a strong difference in behavior between the chlorides and the larger Z halides.

Figure 2. Top: Velocity profiles for Cl and Cl* following irradiation of room temperature NaCl at 7.5 eV. Bottom: Kinetic energy distributions for Cl and Cl*.

We also have successfully measured the hyper-thermal atomic emission from hydrothermally grown $CaCl_2$ crystals and KBr powders, so these results are not confined to alkali halide single crystals. Our model and technique appear to be as general as hyperthermal emission due to surface exciton decay.
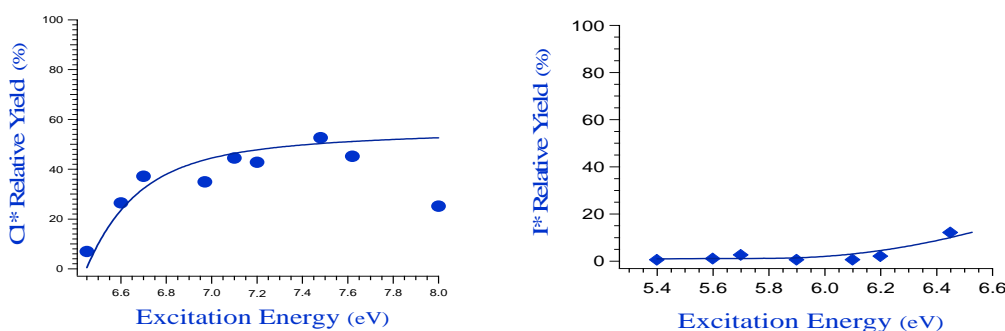

Figure 3. The relative Cl* yield, $\Phi_{Cl^*} = 100 \times [Cl^*]/([Cl]+[Cl^*])$, for NaCl. Left: The relative hyperthermal I*. Right: The relative Br* and I* yield ranges from near zero to <15% from KBr and KI.

References

Beck KM, AG Joly, and WP Hess. 2001. "Evidence for the Surface Exciton in KBr Via Laser Desorption." *Physical Review B* 63:125423-125426.

Hess WP, AG Joly, DP Gerrity, KM Beck, PV Sushko, and AL Shluger. 2002. "Control of Laser Desorption Using Tunable Single Pulses and Pulse Pairs." *Journal of Chemical Physics* 116:8144-8151.

Joly AG, KM Beck, M Henyk, WP Hess, PV Sushko, and AL Shluger. 2003. "Surface Electronic Spectra Detected by Atomic Desorption." *Surface Science* 544:L683-L688.

Atmospheric Aging of Dust

A Laskin,[a] JP Cowin,[b] and MJ Iedema[a]
(a) W.R. Wiley Environmental Molecular Sciences Laboratory, Richland, Washington
(b) Pacific Northwest National Laboratory, Richland, Washington

Dust in the atmosphere not only degrades air clarity, it also can affect our health and influence climate and chemistry of the atmosphere at scales ranging from regional to global. Whether a dust particle will injure the lungs, help form a cloud, or adsorb or scatter light depends on the chemical and physical properties of the particle. These chemical and physical properties constantly evolve from the moment of origin of the particle to its eventual removal from the atmosphere, typically days later. We may have some knowledge about the composition and properties of dust particles at the moment they enter the atmosphere (e.g., the origin of the particles could be known—fresh sea-water mist, mineral/soil dust, or diesel exhaust); however, much less is known about the evolution of these particles as they age.

In this project, our research team is studying the aging of particles in the atmosphere and its impact on our atmospheric environment. The studies include both laboratory and field measurements and involve a number of external collaborators. We use our novel automated sampler (Laskin et al. 2003a) to collect time-resolved dust samples in different environments, and then we analyze the individual particles in our laboratories using state-of-the-art, computer-controlled scanning electron microscopy with elemental analysis via emitted x-rays and time-of-flight secondary ion mass spectrometry. Many of these projects benefit from the capabilities of the electron microscope, which permit imaging the particles under conditions that are representative of those in the natural environment—for example, relative humidity up to 100% or when several Torr of reactive gases are present.

In a collaborative study with the group of VH Grassian (University of Iowa), we studied the chemistry of aerosol particles reacting with HNO_3, a pervasive gas-phase species in polluted industrial areas. Changes observed for SiO_2, $CaCO_3$, $NaCl$, and sea-salt particles following reaction with HNO_3 vapor are shown in Figure 1. The images in row (a) show a SiO_2 particle before and after exposure to HNO_3. The SiO_2 particles are unreactive to the HNO_3. The images in row (b) show how calcium carbonate dust reacts rapidly, and its x-ray emission spectrum (not shown) confirms its transformation to a calcium nitrate product (Krueger et al. 2003b). The images in rows (c) and (d) show the morphological changes of $NaCl$ and sea-salt particles. The $NaCl$ particles show a modest formation of $NaNO_3$ microcrystallites on the particle surfaces, while the sea-salt particles reacted to near completion. These transformations are accelerated greatly by the hydroscopic nature of the product compounds (especially calcium and magnesium nitrate), and are expected to greatly alter the lifetime and ability to seed clouds of common atmospheric dusts (Krueger et al. 2003a, 2003b).

In a collaborative study with the group of BJ Finlayson-Pitts (University of California, Irvine), we probed the composition of NaCl particles reacted with hydroxyl radicals (Laskin et al. 2003b). We showed that the hydroxyl radicals transformed sea-salt dust into both perchlorates and hydroxides via reactions with interfacial chloride ions. In the marine boundary layer, these reactions lead to an increased particle alkalinity that, in turn, will lead to an increase in the uptake and oxidation of SO_2 to sulfate in sea-salt particles. Based on our first-order calculations, we believe that this chemical process may have an important impact on the atmosphere in remote marine areas.

Other ongoing collaborative projects include aging of diesel exhaust particles with MJ Molina and LT Molina (Massachusetts Institute of Technology), characterization and aging of biomass burning particles with WC Malm and JL Hand (National Park Service and Colorado State University, respectively), and characterization of aerosols collected with personal samplers in New York schools with S Chillrud and P Kinney (Columbia University).

Figure 1. Secondary electron images of single particles before and after reaction with gaseous nitric acid (HNO_3) and water vapor. (a) SiO_2 before and after exposure to 1 Torr HNO_3 and ~25% relative humidity for 20 minutes. (b) $CaCO_3$ before and after exposure to 20 μTorr HNO_3 and 41% relative humidity for 4 hours. (c) NaCl before and after exposure to 20 μTorr HNO_3 and 17% relative humidity for 5 hours. (d) Sea salt before and after exposure to 20 μTorr HNO_3 and 17% relative humidity for 5 hours. Adopted from Krueger et al. 2003a.

References

Krueger BJ, VH Grassian, MJ Iedema, JP Cowin, and A Laskin. 2003a. "Probing Heterogeneous Chemistry of Individual Atmospheric Particles Using Scanning Electron Microscopy and Energy Dispersive X-Ray Analysis." *Analytical Chemistry* 75:5170-5179.

Krueger BJ, VH Grassian, A Laskin, and JP Cowin. 2003b. "Laboratory Insights into the Processing of Calcium Containing Mineral Dust Aerosol in the Troposphere." *Geophysical Research Letters* 30:1148-1151.

Laskin A, MJ Iedema, and JP Cowin. 2003a. "Time-Resolved Aerosol Collector for CCSEM/EDX Single-Particle Analysis." *Aerosol Science and Technology* 37:246-260.

Laskin A, DJ Gaspar, W-H Wang, SW Hunt, JP Cowin, SD Colson, and BJ Finlayson-Pitts. 2003b. "Reactions at Interfaces as a Source of Sulfate Formation in Sea-Salt Particles." *Science* 301:340-344.
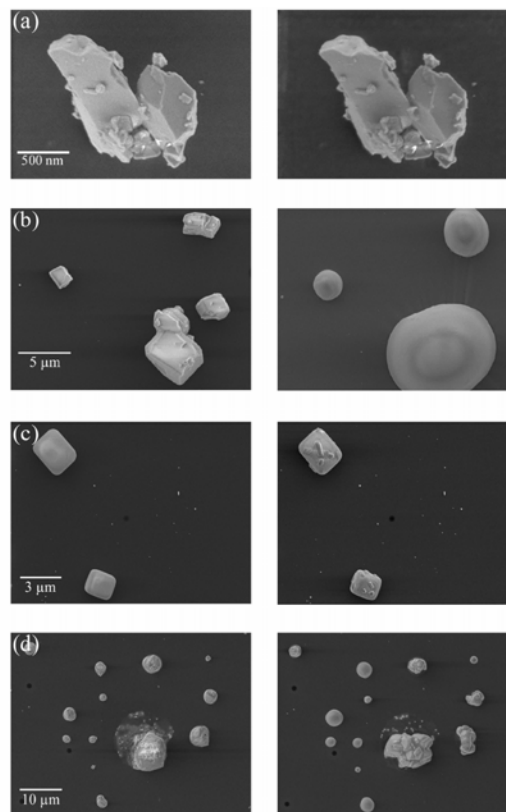
Probing Nano-Planets

JP Cowin,[a] MJ Iedema,[b] G Schenter,[a] RC Bell,[c] and HF Wang[a]
(a) Pacific Northwest National Laboratory, Richland, Washington
(b) W.R. Wiley Environmental Molecular Sciences Laboratory, Richland, Washington
(c) Pennsylvania State University, Altoona Campus, Pennsylvania

What is a nano-planet? The term "nano-planet" is a fanciful way to describe the micron-sized dust in a nebula around a newborn star that may some day agglomerate to form planets. The qualifying statement "…may some day agglomerate to form planets" is emphasized, because the new star's stellar wind also begins to slowly strip the nebula of this dust. A planet must form within 1 million years, or the dust supply will be gone.

To understand how this process occurs, scientists need to determine how the dust can agglomerate fast enough to reach gravitationally bound "planetesimals" that are tens of meters in size. Our studies of the properties of low-temperature water ices have given us insight into that process. Water ice is a very plentiful material in these nebulae, and most dust grains will be heavily coated with water ice, or even largely composed of water ice. Unlike the normal ice we know on earth, most of this ice forms amorphously via condensation from the vapor state straight to the solid state at very low temperatures (10 to 100 K). At these temperatures, the water dipoles tend to slightly align, creating strong electrostatic fields within or around the ice grains (see Figure 1). Even in the presence of neutralizing ions, collisions and temperature changes re-expose the electric fields, which greatly enhance the sticking rate of the ice grains. We also measured the elastic properties of the low-temperature ice. As shown in Figure 1, it is very inelastic, which also makes it much easier for two colliding icy grains to stick together.
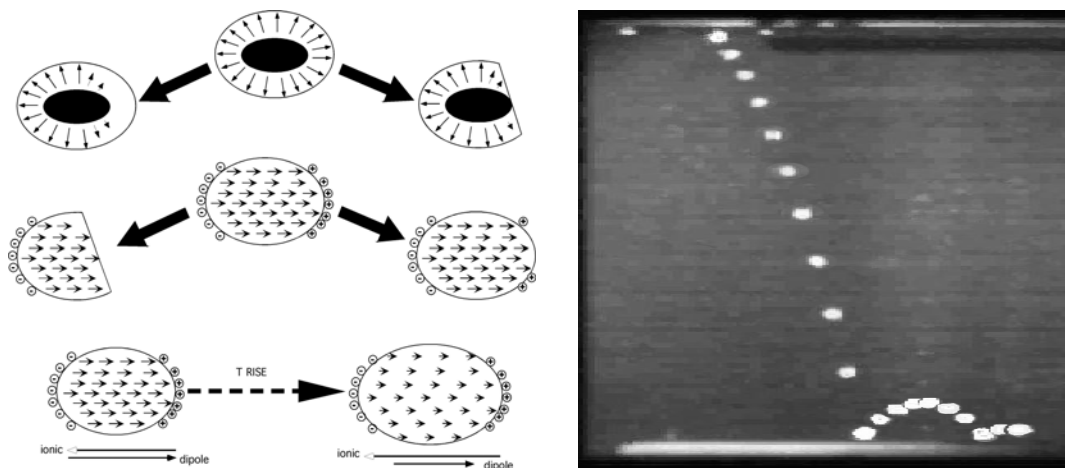

Figure 1. Left: Icy grains in pre-planetary nebula acquire electrostatic charges or dipoles because of the unique tendencies of low-temperature ice to spontaneously polarize (top), spew charged fragments after collisions (middle), or polarize via subtle T-induced charge imbalances (bottom). Right: Time-lapse photo of a ball bouncing from a slab of amorphous ice demonstrates the inelasticity of this low-temperature ice.

Probing Nano-Fluids

JP Cowin,[a] MJ Iedema,[b] RC Bell,[c] and HF Wang[a]
(a)   Pacific Northwest National Laboratory, Richland, Washington
(b)   W.R. Wiley Environmental Molecular Sciences Laboratory, Richland, Washington
(c)   Pennsylvania State University, Altoona Campus, Pennsylvania

Very small chunks of matter and the periphery region of large chunks often have properties so different from the bulk that bulk properties are poor predictors of processes occurring in those regions. Examples of this phenomenon are found within nanometers of a fluid interface, in fluids found within nanophase materials, in the ubiquitous aqueous films sorbed on most hydrophilic materials, and in atmospheric dust. In this research, we used a unique approach to study interfacially perturbed materials: a soft-landing ion source and molecular beam epitaxy together allow us to re-create liquid-liquid interfaces with high precision. As shown in Figure 1, we grew thin films of solvent at cryogenic temperatures. While the conditions were still too cold for any diffusion to occur, we very gently added a fraction of a monolayer of molecular ions to the film (in this case, hydronium). These ions can be inserted at will at any precise, initial location in the solvent (3-methylpentane) film. We then warmed the film, and followed the motion of the ion with great precision using an electrostatic Kelvin probe. As shown on the right, as we warmed the film, we found that the motion at the top of the film occurs at too low a temperature (as expected for bulk 3-methylpentane), and too high a temperature at the bottom. By using a variety of custom films, we were able to show that the film is orders of magnitude less viscous at the top of the film when compared to the bulk material, and orders of magnitude more viscous at the bottom (Bell et al. 2003).
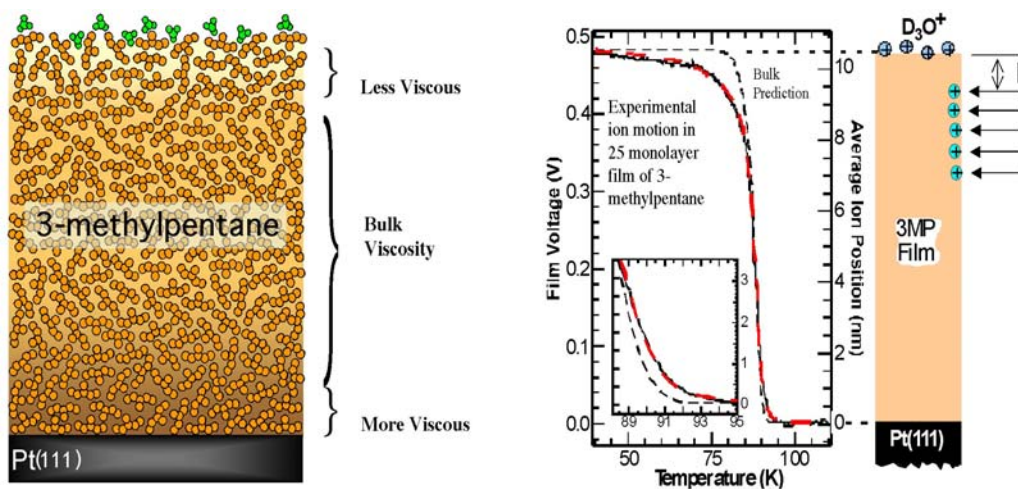

Figure 1. Left: The predictions based on the properties of a bulk material need not apply to the regions that are within the perturbation range of the interface. Right: Quantitative measurements of this effect reveal that its reach is about 2 nanometers.

Reference

Bell R, HF Wang, K Wu, MJ Iedema, and JP Cowin. 2003. "Nanometer-Resolved Interfacial Fluidity." *Journal of the American Chemical Society* 125:5176-5185.

Biological Applications of Imaging Micro- and Nano-Scale Metal Oxides Using Multiphoton Microscopy

G Holtom,[a] Y Gorby,[b] J McLean,[b] and Y Zheng[b]

(a)   W.R. Wiley Environmental Molecular Sciences Laboratory, Richland, Washington
(b)   Pacific Northwest National Laboratory, Richland, Washington

Despite the enormous research activity involving live-cell imaging using fluorescent material and continuing improvements in methods and instrumentation, a number of characteristic problems remain that limit the quality of three-dimensional images in long-duration imaging. These problems are fundamentally related to the physics of the organic chromophores that are usually employed, and appear as photo-bleaching or as photo-induced damage to the cells. We are investigating several technologies involving multiphoton microscopy methods, including coherent anti-Stokes Raman scattering (CARS) and two- and three-photon excitation of fluorescence. Metal oxides, in the form of sub-micron-sized particles (i.e., micro-scale) or sub-100-nm particles (i.e., nano-scale), are resistant to photobleaching but require engineering to avoid particle aggregation. These non-fluorescent species require new nonlinear optical methods for detection, but several metal oxides, particularly several forms of iron oxide, have special relevance to bacterial growth, especially under anerobic conditions.

We are particularly interested in the role of iron oxides in anaerobic metabolism of *Shewanella oneidensis*, an organism capable of reducing metal oxides. This capability potentially could be used to stabilize toxic or radioactive soluble oxides in the aqueous subsurface, thereby rendering them insoluble and reducing their hazard. A number of imaging technologies can be used, with various resolutions, but in general, there is a need for a high-sensitivity, high-resolution method that can be used to image live bacterial cultures. An example of the image quality that can be obtained quickly (a few seconds per high resolution image slice) is given in Figure 1, which shows the simultaneous imaging of fluorescent-labeled *S. oneidensis* and the ferric oxide substrate. Optical images can be produced in closed optical cells, to control oxygen levels, with controlled flow and nutrient characteristics, for long time durations.
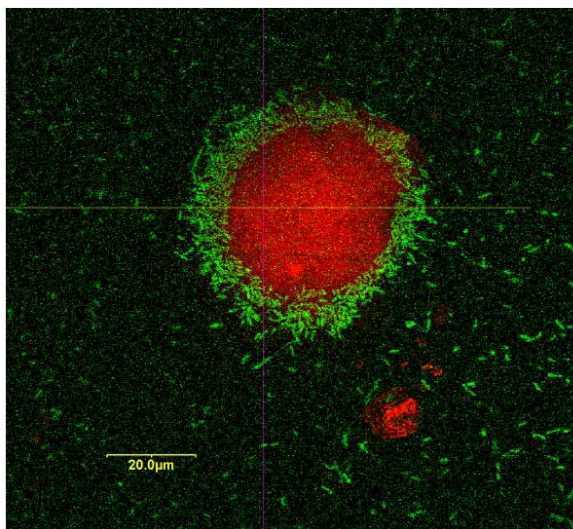

Figure 1. *S. oneidensis* bacteria, labeled with green-fluorescent protein, are imaged by two-photon fluorescence (green channel). The red channel is a CARS image of hydrous ferric oxide (HFO). In this image slice, we see the bottom of a large HFO particle with the bacteria growing in a thin layer between the HFO and the glass cover slip.

The materials science community has been interested in the nonlinear optical properties of iron oxides for at least the last decade, although the measurements involve detection techniques other than the CARS method (Hashimoto et al. 1996). The nonlinear optical susceptibility $\chi^{(3)}$ is the largest of all inorganic oxides reported to date, although other metal oxides have properties that are useful and may be valuable for bio-imaging.

Another metal oxide of interest is ZnO, an n-type semiconductor analogous to the II-VI materials used in quantum dots, such as CdS. The relationship between the fluorescence properties and sizes of these materials are widely known in quantum dot studies (Parak et al. 2003), and the sensitivity of the fluorescence to the local environment is widely considered to be a problem that can be solved through engineering. We are more interested in using the fluorescence properties of ZnO as a probe of the local environment, particularly to report the concentrations of small chemical species such as nutrients and metabolites that are not visible directly, but which play an important role in the development of biofilms. An example of imaging capability is shown in Figure 2.
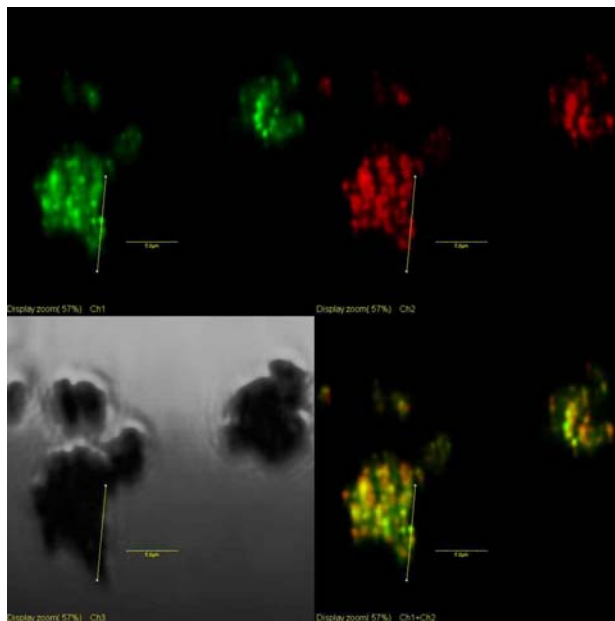

Figure 2. ZnO microparticles placed on a cover slip. The image at the upper left shows green fluorescence, and the image at the upper right is the CARS signal. The lower-left image is a bright field image and the lower-right image is a composite. A 5-μm scale bar is shown, along with a vertical reference mark.

References

Hashimoto T, T Yamada, and T Yoko. 1996. "Third-Order Nonlinear Optical Properties of Sol–Gel Derived α-Fe$_2$O$_3$, γ-Fe$_2$O$_3$, and Fe$_3$O$_4$ Thin Films." *Journal of Applied Physics* 80(6):3184-3190.

Parak WJ, D Gerion, T Pellegrino, D Zanchet, C Micheel, SC Williams, R Boudreau, MA Le Gros, CA Larabell, and AP Alivisatos. 2003. "Biological Applications of Colloidal Nanocrystals." *Nanotechnology* 14:R15–R27.

Shattering of Peptide Ions on Surfaces

J Laskin,[a] TH Bailey,[b] and JH Futrell[a]

(a)   Pacific Northwest National Laboratory, Richland, Washington
(b)   University of Delaware, Newark, Delaware

Ion-surface impact, occurring on a timescale of a few picoseconds following surface impact, is a fast and efficient means for exciting vibrational modes in the projectile molecule. Extensive studies on collision-induced dissociation (CID) and surface-induced dissociation (SID) of small peptides conducted in our laboratory have demonstrated that both methods of collisional activation produce vibrationally excited ions with quasi-thermal distributions of internal energies (Laskin and Futrell 2002). Consequently, low-energy CID and SID mass spectra of small peptides are very similar; however, this is not the case for large peptides that require relatively high collision energy for fragmentation. It has been suggested that this difference between low-energy CID and SID spectra of large peptides is a result of a longer observation time of trapping instruments that are commonly used in CID studies compared to typical SID instruments that sample fragmentation occurring on a microsecond time scale. In this study SID is coupled with Fourier transform ion cyclotron resonance (FTICR) mass spectrometry. This approach allows sampling of much longer reaction times (from hundreds of microseconds to many seconds) and conducting kinetics studies to investigate the time dependence of peptide fragmentation.

For peptides that exhibit selective fragmentation, only a small number of fragments (2 to 5) are observed at low collision energies, and a large number of fragments (>50) are observed at high collision energies. There is also a very sharp transition between the two regimes. Figure 1 is a typical plot of the increase in the number of ions in SID spectra with collision energy. The inset mass spectra are typical of three distinct energy regimes in the SID spectra. At the lowest energy (below 10 eV), only inelastically scattered primary ions are observed. At higher energies (15 to 25 eV), a plateau region is observed for which the lowest energy fragmentation processes, described well by our RRKM model, are represented in SID spectra. At 30 eV, a sharp transition is observed, and spectra above this energy contain a large number of fragments.
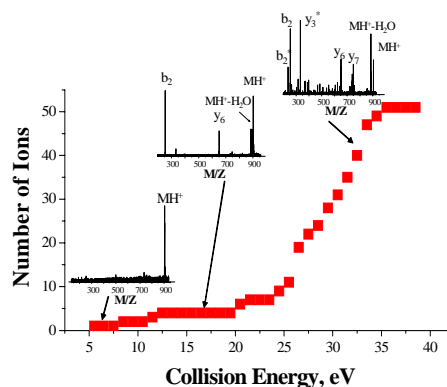

Figure 1. Number of peaks in SID spectrum of des-Arg[9]-bradykinin as a function of collision energy.

A large number of ions at higher collision energy can be formed either from the natural branching of the fragmentation by secondary reactions of primary (low-energy) product ions or from opening up of new competing dissociation pathways. Detailed examination of relative abundances, appearance energies, and kinetic behaviors of different fragment ions demonstrates that most of the fragments observed at high collision energies originate

directly from the excited parent ion. Time-resolved data are obtained by varying ion collision energy and reaction time and plotting the relative abundance of each ion as a function of collision energy for each fragmentation delay. Typical results obtained for des-Arg^9-bradykinin and its selected fragment ions are shown in Figure 2. Fragmentation efficiency curves for the precursor ion and all primary fragments are strongly dependent on the reaction time, while the curves for most of the high-energy fragments do not show any time dependence. Obviously, the time-independent fragments are formed by fast fragmentation of the excited precursor ion and not by consecutive dissociation of the primary fragments. This fast fragmentation is unexpected for large peptides with 350 to 600 internal degrees of freedom. RRKM modeling of experimental data using the

Figure 2. Time- and energy-resolved curves for the parent ion and selected fragments of des-Arg^9-bradykinin for different reaction delays.

approach developed by our group (Laskin and Futrell 2003) using two decay rates (slow and fast) demonstrated that fast fragmentation could be modeled with the so-called "sudden death" approximation in which the molecule fragments instantaneously after reaching a certain threshold.

Instantaneous fragmentation of large molecules at high collision energies occurs on or very near the surface rather than in the gas phase and indicates a transition in the dynamics of ion-surface interaction—namely, the shattering transition. Although transition from recoil to shattering has been reported for cluster ions, this study presents the first experimental evidence for shattering of peptide ions on fluorinated self-assembled monolayer surfaces. Coupling SID with FTICR mass spectrometry allowed us to distinguish between the effects of observation time window and the transition in dynamics of peptide ion-surface interaction on fragmentation patterns of protonated peptides.

References

Laskin J and JH Futrell. 2002. "On the Efficiency of Energy Transfer in Collisional Activation of Small Peptides." *Journal of Chemical Physics* 116:4302-4310.

Laskin J and JH Futrell. 2003. "Collisional Activation of Peptide Ions in FT-ICR Mass Spectrometry." *Mass Spectrometry Reviews* 22:158-181.
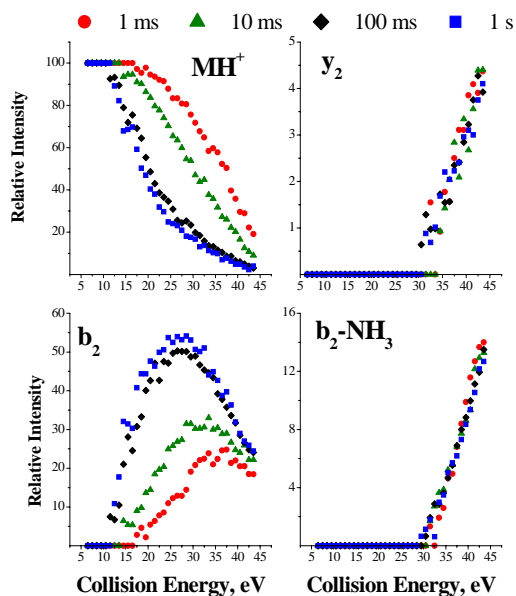
Soft-Landing of Large Ions on Self-Assembled Monolayer Surfaces

J Alvarez,[a] RG Cooks,[a] J Laskin,[b] SE Barlow,[c] D Gaspar,[c] and JH Futrell[b]

(a)   Purdue University, West Lafayette, Indiana
(b)   Pacific Northwest National Laboratory, Richland, Washington
(c)   W.R. Wiley Environmental Molecular Sciences Laboratory, Richland, Washington

Soft-landing of ions on surfaces (deposition of intact ions) is a process that occurs in collision of low-energy ions (<10 eV) with carefully selected semiconductive surfaces. Soft-landing experiments have been reported for small closed-shell ions (Miller et al. 1997), oligonucleotides (Feng et al. 1999), and, most recently, for multiply protonated proteins (Ouyang et al. 2003). Most of these experiments utilized self-assembled monolayer (SAM) surfaces or liquid surfaces (Wu et al. 2000). SAM surfaces facilitate efficient dissipation of the initial kinetic energy of the ion, prevent ion neutralization by charge reduction or proton transfer, and minimize ion-molecule reactions on the surface. It has been proposed that soft-landing of proteins could be used for generating protein microarrays. Similarly, peptide microarrays can be produced using soft-landing. Further, peptide ions present an ideal model system for studying the fundamental aspects of soft-landing of large ions on SAM surfaces.

Our studies used a 6-T Fourier transform ion cyclotron resonance (FTICR) mass spectrometer both for ion deposition on surfaces and for the *in situ* analysis of SAM surfaces following soft-landing. Low-energy (<10 eV), mass-selected ions were deposited on fluorinated SAM (FSAM) surfaces. Surface analysis was performed by impacting the surface with a 2-kV Cs^+ ion beam generated by an ion gun positioned on the instrument axis in combination with gated trapping of desorbed ions. Efficient trapping of desorbed ions is facilitated by using high (30-V) trapping potential, which is a unique feature of our ICR cell.

Figure 1 shows 2-kV Cs^+ secondary ion mass spectroscopy (SIMS)-FTICR mass spectra of the FSAM surface before soft-landing (Figure 1 [left]) and after soft-landing of doubly-charged bradykinin $[M+2H]^{2+}$ (Figure 1 [right]). In both mass spectra, the base peak corresponds to reactive scattering of gold with a CF_2^+ group. Peaks observed in the SIMS-FTICR mass spectrum of the FSAM surface (Figure 1 [left]) corresponding to fragments of the FSAM surface and gold clusters are typical for SIMS analysis of FSAM surfaces. The SIMS-FTICR mass spectrum shown in Figure 1 (right) was obtained after soft-landing of 10-eV ions of doubly protonated bradykinin for 1 hour. The main feature of this mass spectrum is the presence of the mass peak corresponding to the singly protonated species and a series of peaks corresponding to fragment ions of the peptide. By comparing the relative intensities of peptide peaks in this spectrum to fragmentation patterns of doubly protonated bradykinin obtained using surface-induced dissociation (SID), we conclude that 2-kV Cs^+ SIMS yields the same internal energy deposition as 50-eV inelastic collision of the intact peptide with the FSAM surface. However, SIMS spectra also contain peptide fragments that are not observed using SID. Fragment ions a_5 and c_5 are typically observed in high-energy, collision-induced dissociation (CID) spectra.
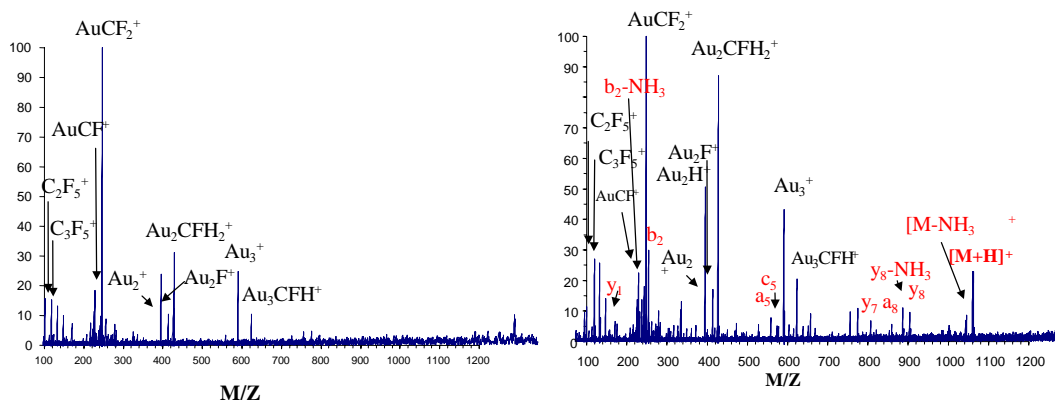
Figure 1. 2-kV Cs$^+$ SIMS FTICR mass spectra of the FSAM surface before soft-landing (left) and after soft-landing of the doubly protonated bradykinin (right).

Similar results were obtained using 15-kV Ga$^+$ time of flight (TOF)-SIMS for surface analysis. For these experiments, samples were prepared in the FTICR mass spectrometer and transferred into the TOF-SIMS instrument within 1 hour after soft-landing. These successful *ex situ* analysis experiments demonstrated that soft-landed ions are fairly tightly bound to the FSAM surface. However, signals associated with soft-landed ions degraded as a function of time even when surfaces were stored under ultrahigh vacuum conditions following their exposure to the ion beam.

Experiments were conducted to explore the effect of the initial charge state of the precursor ion on the efficiency of soft-landing by dosing the same amount of doubly and triply protonated substance P on the FSAM surface. We found that for both charge states of the precursor [M+H]$^+$ ion is a dominant peptide-related peak in 2-kV Cs$^+$ SIMS spectra. However, the relative abundance of the [M+H]$^+$ peak in SIMS spectra is two to three times higher for the triply protonated precursor ion. Does the efficiency of soft-landing increase with charge state? Does the proton loss occur during soft-landing or during SIMS analysis? What is the effect of the initial velocity of the precursor ion on soft-landing? These questions will be addressed in detail in our future studies.

References

Feng BB, DS Wunschel, CD Masselon, L Pasa-Tolic, and RD Smith. 1999. "Retrieval of DNA Using Soft-Landing after Mass Analysis by ESI-FTICR for Enzymatic Manipulation." *Journal of the American Chemical Society* 121:8961-8962.

Miller SA, H Luo, SJ Pachuta, and RG Cooks. 1997. "Soft-Landing of Polyatomic Ions at Fluorinated Self-Assembled Monolayer Surfaces." *Science* 275:1447-1450.

Ouyang Z, Z Takats, TA Blake, B Gologan, AJ Guymon, JM Wiseman, JC Oliver, VJ Davisson, and RG Cooks. 2003. "Preparing Protein Microarrays by Soft-Landing of Mass-Selected Ions." *Science* 301:1351-1354.

Wu K, MJ Iedema, and JP Cowin. 2000. "Ion Transport in Micelle-Like Films: Soft-Landed Ion Studies." *Langmuir* 16:4259-4265.

Full-Color Emission in Poly-P-Phenylene Ethynylene-ZnS:Mn^{2+} Composite Particles

W Chen,[a] AG Joly,[b] J-O Malm,[c] J-O Bovin,[c] and S Wang[a]

(a)   Nomadics, Inc., Stillwater, Oklahoma
(b)   Pacific Northwest National Laboratory, Richland, Washington
(c)   University of Lund, Sweden

Currently, nanostructured materials form a new branch of materials science under extensive investigation. For semiconductor nanoparticles, perhaps the most striking property of these materials is the massive change in optical properties as a function of size, most notably observed as a blue shift in the absorption spectrum with the decrease of the particle size. As the particle size approaches the exciton Bohr radius, there are drastic changes in the electronic structure and the physical properties (e.g., a shift of the energy levels to higher energy; the development of discrete features in the spectra; and concentration of the oscillator strength into just a few transitions). These novel characteristics enable semiconductor nanoparticles to have a bright future in practical applications such as lasers, flat panel displays, optical storage, single electron transistors, and biological probes.

Often during nanoparticle preparation, organic polymers are used to terminate particle growth, allowing fabrication of nanocomposites, which is a new class of composite materials consisting of organic polymers and inorganic nanoparticles. In nanocomposites, the organic polymer has two functions; it stabilizes the nanoparticles and couples the organic and the inorganic components, usually resulting in materials with novel properties and applications. Recently, for example, highly fluorescent polymer particles composed of anionic poly(phenylene ethynylene) (aPPE) have been used to capture Cy-5 labeled oligonucleotides (Moon et al. 2003). These aPPE particles may find applications in displays and lighting because they have a strong blue emission, peaking at 460 nm.

The aPPE/ZnS:Mn^{2+} nanocomposites are composed of 500-nm aPPE crystallites and 4.5-nm ZnS:Mn^{2+} nanoparticles. Figure 1 shows the emission spectra of the nanocomposite particles. The strongest peak in the emission spectrum at 460 nm is attributed to the origin band emission in the aPPE polymer (Moon et al. 2003; Yang et al. 1998). The emission shoulder at 490 nm may be from an excimer formed within the polymer (Moon et al. 2003; Yang et al. 1998). The peak at 596 nm is assigned to a well-known transition in Mn^{2+}, while the peak at 700 nm is due to a defect emission in the ZnS.
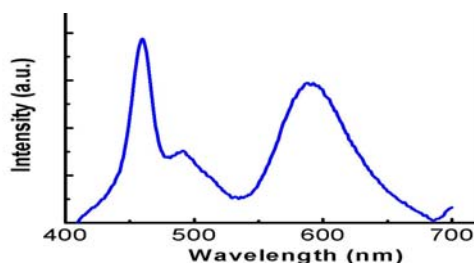

Figure 1. Luminescence spectrum of the aPPE/ZnS:Mn^{2+} nanocomposite material. The peaks at 460 and 490 nm are assigned to aPPE, while the peak at 596 nm is assigned to Mn^{2+}. The peak at 706 nm is attributed to a defect in the ZnS.

As displayed in Figure 2, the overall emission color of the nanocomposite changes for different excitation wavelengths because the relative emission intensities of Mn^{2+} and aPPE particles change. As shown in the figure inset, as the excitation wavelength varies from 280 to 420 nm, the orange (596 nm) emission intensity of Mn^{2+} decreases, while the blue (460 nm) and green (490 nm) emissions of aPPE particles increase. This change in intensity is related to the energy structure of $ZnS:Mn^{2+}$ nanoparticles and aPPE particles in the composite. The conduction band of aPPE particles partially overlaps with the excited states of $ZnS:Mn^{2+}$ nanoparticles, while the energy gap of $ZnS:Mn^{2+}$ nanoparticles (around 330 nm) is larger than that of aPPE particles (around 420 nm). In this case, if the excitation energy is greater than the energy gap of $ZnS:Mn^{2+}$ nanoparticles, the induced emission is mainly from Mn^{2+} particles, and the emission of Mn^{2+} is stronger than that of aPPE particles in intensity. If the excitation energy is less than the energy gap of the $ZnS:Mn^{2+}$ nanoparticles but greater than the energy gap of aPPE particles, the induced emission is mainly from aPPE particles. If the excitation energy is less than the energy gap of $ZnS:Mn^{2+}$ nanoparticles, the emission of Mn^{2+} may be due to the excitation of d–d transitions of Mn^{2+}. As the d–d absorption cross section of Mn^{2+} is smaller than the band-to-band transition of ZnS, the d–d excited luminescence is weaker in intensity than that from the band-to-band excitation. This phenomenon provides a possible mechanism to adjust the emission color of the composite by varying the excitation wavelength, thus making these materials useful in applications involving emission displays.
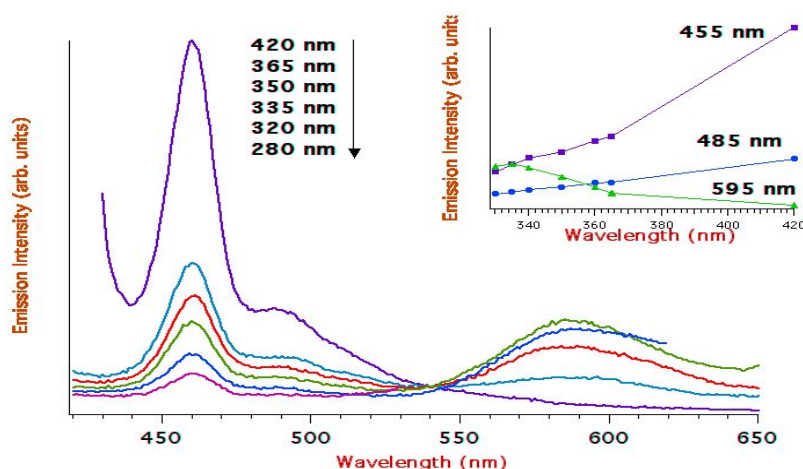

Figure 2. Photoluminescence spectra of the aPPE/ZnS:Mn^{2+} nanocomposite following excitation at different wavelengths. The inset displays the variation in luminescence intensity of the different emissions as a function of excitation wavelength.

References

Moon JH, R Deans, E Krueger, and LF Hancock. 2003. "Capture and Detection of a Quencher Labeled Oligonucleotide by Poly(phenylene ethynylene) Particles." *Chemical Communications* 1:104-105.

Yang JS and TM Swager. 1998. "Fluorescent Porous Polymer Films as TNT Chemosensors: Electronic and Structural Effects." *Journal of the American Chemical Society* 120:11864-11873.

Helium Diffusion through H_2O and D_2O Amorphous Ice: Observation of a Lattice Inverse Isotope Effect

JL Daschbach,[a] GK Schenter,[b] P Ayotte,[c] RS Smith,[b] and BD Kay[b]

(a)   *W.R. Wiley Environmental Molecular Sciences Laboratory, Richland, Washington*
(b)   *Pacific Northwest National Laboratory, Richland, Washington*
(c)   *Université de Sherbrooke, Sherbrooke (Québec), Canada*

Isotopic substitution has long been an invaluable tool for determining the details of a reaction or diffusion mechanism. The effects of isotopic substitution are typically classified as primary or secondary depending on whether the substituted atom is directly or indirectly involved in the process. For hydrogen atom substitution, it is generally observed that processes occur faster with the lighter isotope ($Rate_H > Rate_D$). There are, however, a few cases for which the rates are faster with the heavier isotope ($R_D > R_H$); this is referred to as an inverse isotope effect. For example, the diffusion of deuterium atoms is faster than hydrogen atoms in both palladium and polycrystalline H_2O ice. In these systems, the isotopic composition of the diffusing species is responsible for the effect; hence, they exhibit a primary inverse isotope effect.

In this work, we have observed an inverse isotope effect, not for the diffusing species, but for the isotopic composition of the solid lattice. To our knowledge, this is the first observation of an inverse isotope effect for diffusion in a solid where the isotopic mass change occurs in the lattice. Transition state theory (TST) calculations are consistent with the experimental observations and suggest that the observed inverse isotope effect is caused by a tight transition state. This state results in a large difference in the vibrational zero-point energy between the reactant and transition state configurations of helium in the water lattice. This isotope effect arises predominantly from frustrated rotations of the H_2O (D_2O) molecules comprising the lattice water.

Figure 1 shows temperature programmed desorption (TPD) spectra for desorption of helium implanted in 6 ML amorphous solid water (ASW) and capped with a series of H_2O and D_2O ASW overlayers of increasing thicknesses. For both H_2O and D_2O, the helium TPD peak broadens monotonically with increasing cap thickness and moves to higher temperature. The observed broadening with thickness is the expected behavior for diffusive transport through the overlayer. For a fixed cap thickness, the He TPD peak in D_2O is observed at a lower temperature than in H_2O, indicating that the He diffusion through D_2O is faster than through H_2O.
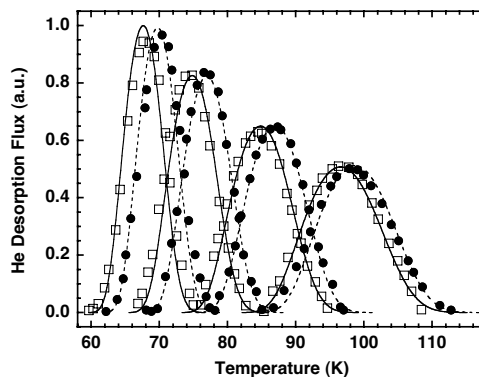

Figure 1. The TPD of He implanted ASW H_2O (circles) and D_2O (squares) capped with 80, 240, 800, and 2400 ML of ASW. The lines through the data are Arrhenius fits [H_2O (dashed), D_2O (solid)] using a one-dimensional, kinetic-hopping model.

The data in Figure 1 clearly demonstrate that He diffuses faster through D_2O than through H_2O. Additional experiments (data not shown) performed using $H_2^{18}O$ ASW show that helium diffusion through $H_2^{16}O$ and $H_2^{18}O$ are indistinguishable. This result rules out translational diffusive motion of the ASW as the source of the observed isotope effect. Recent studies of self diffusion in ASW are consistent with a translationally static lattice at these temperatures (Smith et al. 1999, 2000).

To provide a semi-quantitative physical understanding of the observed lattice isotope, we performed TST calculations to calculate the diffusion rate through a model ice lattice composed of 16 water molecules with periodic boundary conditions. Figure 2 displays the cumulative free energy, ΔG_i, as a function of vibrational mode index, i, for H_2O (dashed line), D_2O (solid line), and $H_2^{18}O$ (circles). The total ΔG (the sum over all vibrational modes, the value at mode index 96) is the free energy difference between the reactant minimum and the transition state, and is thus related to the diffusion rate. A larger ΔG means a slower diffusion rate and vice versa. The calcula-

Figure 2. TST calculated cumulative ΔG versus the vibrational mode index mode for D_2O (solid line), H_2O (dashed line), and $H_2^{18}O$ (circles). The vertical line separates the frustrated translations (1-48) and the frustrated rotations (49-96).

tions predict, in agreement with the experiments, that He diffusion will be fastest in D_2O and that diffusion in $H_2^{16}O$ and $H_2^{18}O$ will be nearly identical. The plot also reveals the origin of the observed lattice inverse isotope effect. The value of ΔG after the summation over all of the frustrated translational modes is given at mode 48, which is the last frustrated translation. At this point, the difference between ΔG for the three species is small. However, when the frustrated rotations are added in (modes 49 through 96), the ΔGs for H_2O and $H_2^{18}O$ clearly diverge from the value for D_2O. Thus the difference in free energy clearly arises from the vibrations associated with the frustrated rotations of the lattice water.

The combined experimental and theoretical evidence outlined above clearly show the existence of a previously unobserved lattice inverse isotope effect for diffusion in a solid. The transition state calculations successfully predict that He diffusion is more rapid in D_2O than in H_2O and that there is no difference between $H_2^{16}O$ and $H_2^{18}O$. Further, it provides a physical explanation for the source of the lattice (secondary) inverse isotope effect, namely the frustrated rotations of the water lattice.

References

Smith RS and BD Kay. 1999. "The Existence of Supercooled Liquid Water at 150 K." *Nature* 398(6730):788-791.

Smith RS, Z Dohnalek, GA Kimmel, KP Stevenson, and BD Kay. 2000. "The Self-Diffusivity of Amorphous Solid Water Near 150 K." *Chemical Physics* 258(2-3):291-305.
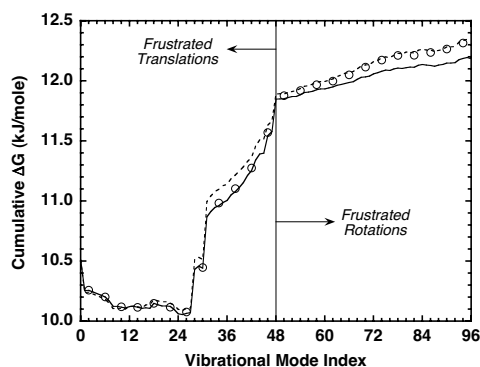
Pd Nanoclusters Supported on MgO(100): Effects of Cluster Size on Chemisorption Properties

S Tait,[a] CT Campbell,[a] BD Kay,[b] and Z Dohnálek[b]
(a)   University of Washington, Seattle, Washington
(b)   Pacific Northwest National Laboratory, Richland, Washington

Because of research on model catalyst systems during the last decade, much progress has been made in understanding supported metal catalysts at the nanometer scale. By studying these model systems, improvements in the efficiency and cleanliness of industrial chemical reactions can be accomplished. Understanding the effect that the nanometer-scale confinement of matter has on catalytic properties is one of the current scientific challenges. Detailed analysis at the nanoscale allows us to probe the atomic-scale interactions of adsorbed metals and their oxide supports, both with each other and with other adsorbed species.

Nanometer-sized Pd particles supported on oxides are active catalysts for a variety of important reactions involving small alkanes. For example, low-temperature combustion of methane allows cleaner energy production because it minimizes NO_x pollution. The intent of this project is to study adsorption of small alkane molecules on MgO(100) and the effects of particle size on the adsorption and dissociation of methane on model catalysts consisting of size-controlled Pd nanoclusters supported on MgO(100).

This work has been done using a sophisticated molecular beam surface scattering apparatus in the W.R. Wiley Environmental Molecular Sciences Laboratory (EMSL) at Pacific Northwest National Laboratory (see Figure 1). This apparatus has a suite of surface science capabilities that are especially important for this project, including three quadruply pumped molecular beams, precise sample position control, precise control of beam angle of incidence on the sample, quadrupole mass spectrometer (QMS) for background measurement, line-of-sight QMS rotating about the sample, precise sample temperature control in

Figure 1. Graduate student from the University of Washington conducts research using the EMSL molecular beam scattering instrument.

the range 20 to 2000 K, Auger electron spectroscopy, x-ray photoelectron spectroscopy, metal vapor deposition sources, a quartz crystal microbalance, and computer-instrument interfacing for automated experiment control.
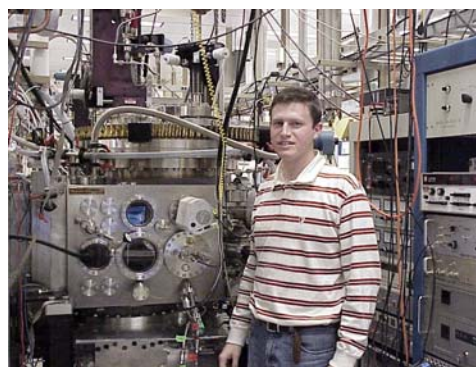
As part of our initial approach to address this problem, we have used molecular beam scattering and temperature programmed desorption (TPD) at low temperatures to study the adsorption and dissociation of hydrocarbons (methane, ethane, butane, hexane, octane, and decane) on MgO(100) thin films. Highly collimated molecular beams of the small alkane molecules are impinged on the sample. We see that the initial sticking probability increases with molecule size up to octane at which point the sticking coefficient is unity. As the size

of the alkane molecule increases, there are more modes available to dissipate the incident kinetic energy of the molecule. The TPD experiments provide information about the adsorption energy of the alkane molecules on the MgO surface.

Figure 2 shows the TPD spectra for a series of small straight chain hydrocarbons from an epitaxially grown MgO(100) thin film. The hydrocarbons are deposited on the substrate at about 20 K, and each spectrum corresponds to one monolayer of the hydrocarbon on the MgO thin film. We observe a clear trend of increasing desorption energy with increasing alkane chain length. The spectra show that the TPD peak shifts to higher temperature with an increasing chain length that is consistent with an increase in binding energy with chain length. However, a more complete analysis of the TPD spectra coupled with the dynamic scattering measurements is needed to provide the quantitative details of the adsorption dynamics and desorption kinetics for hydrocarbon/catalytic surface interactions. The adsorption energy is derived from a measurement of the flux of desorbing molecules as the temperature of the sample is increased at a controlled rate. Our initial analysis also indicates an increase in the pre-exponential factor of the desorption equation. Theoretical modeling is under way to understand this dependence.
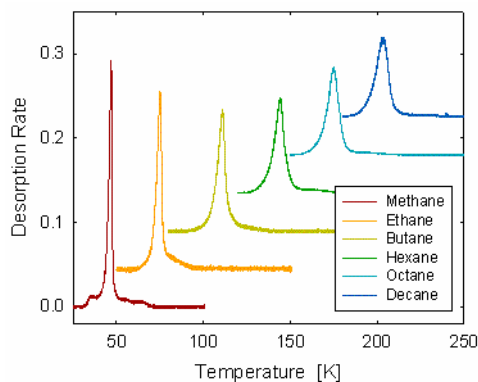

Figure 2. TPD spectra of a series of straight-chain hydrocarbons desorbing from an epitaxially grown MgO thin film. Each spectrum corresponds to one monolayer coverage of the given species.

We have also measured the dissociation of methane on MgO-supported Pd nanoparticles for several Pd coverages and beam energies. Some fraction of the hydrocarbon molecules dissociate as they reach the surface, leaving behind surface carbon. The residual carbon is titrated from the surface with a molecular O_2 beam. Methane sticking is observed to increase exponentially as a function of beam energy on both the Pd particles and on the Pd film. We see that the adsorbed carbon signal on the Pd particles reaches a saturation level much earlier than the signal from the continuous Pd film. This indicates that the breaking of the C–H bond in the small hydrocarbons is more readily accomplished on the Pd nanoparticles than on a continuous Pd surface. These measurements will advance our specific understanding of the catalytic activity of this important combustion catalyst and our general understanding of particle-size effects in hydrocarbon catalysis.

Electron-Stimulated Reactions at the Interfaces of Amorphous Solid Water Films

GA Kimmel[a] and NG Petrik[a]
(a) Pacific Northwest National Laboratory, Richland, Washington

The fundamental mechanisms of radiation damage to molecules in the condensed phase are of considerable interest to fields ranging from radiation biology to astrophysics. In particular, the structure of condensed water and its interactions with electrons, photons, and ions have been extensively studied and a variety of mechanisms for the non-thermal dissociation of water have been identified. However, the dynamics and kinetics of electronic excitations in water and their connection to the radiolysis products of water are still largely unknown.

In this paper, we describe our study of the electron-stimulated production of molecular hydrogen from thin films of amorphous solid water (ASW) grown on Pt(111) as a function of film thickness (Petrik and Kimmel 2003). We show that there are two sources of hydrogen with distinct reaction kinetics. Experiments with isotopically layered films of D_2O and H_2O show that D_2 is produced almost entirely at the two interfaces of the films—the ASW/Pt interface and the ASW/vacuum interface. However, the energy that drives these reactions is absorbed within the bulk of the film. The results suggest that electronic excitations in the bulk of the film diffuse to either interface prior to reacting, and that electron-stimulated reactions are significantly enhanced at interfaces as compared to the bulk.

The experiments were performed in an ultrahigh vacuum system equipped with an electron gun, two effusive gas dosers, and a quadrupole mass spectrometer. Dense, relatively smooth ASW films with surface areas that were approximately independent of film thickness were grown on Pt(111) at 100 K. The ASW films were irradiated at 100 K with 100-eV electrons in 240-s beam pulses.

The D_2 electron-stimulated desorption (ESD) yield as a function of ASW film thicknesses ranging from $0 < \theta < 200$ ML is shown in Figure 1. The D_2 ESD is composed of two components associated with reactions at the ASW/Pt interface and the ASW/vacuum interface. The total D_2 yield has a maximum at $\theta \sim 25$ ML and decreases to a coverage independent value for $\theta > 100$ ML (Figure 1a, solid circles). The D_2 from the ASW/vacuum interface increases monotonically for $\theta < 100$ ML and is constant for higher coverages (Figure 1a, open circles). The D_2 yield from the ASW/Pt interface is initially small, reaches a maximum at $\theta \sim 25$ ML, and then declines to approximately zero for $\theta > 100$ ML (Figure 1b). Note that the thickness over which the D_2 yield change is approximately 100 ML, suggesting that energy deposited into the film contributes to the D_2 ESD yield over that length scale.
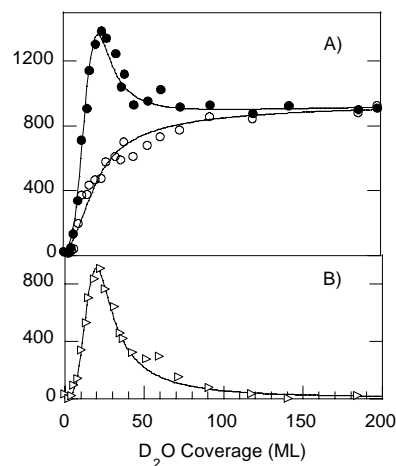

Figure 1. D_2 ESD yield vs. D_2O coverage. a) Solid circles are the total D_2 ESD yield; open circles are the D_2 ESD yield from the ASW/vacuum interface. b) D_2 ESD yield from the ASW/Pt interface.

To investigate where in the films the D_2 is produced, we used isotopically layered films of D_2O and H_2O. Figure 2 shows the D_2 yield from the ASW/vacuum interface for a 20-ML D_2O film as a function of the coverage of the H_2O capping layer (solid circles). The D_2 yield decreases approximately exponentially with increasing H_2O coverage with a *1/e* constant of approximately 2.3 ±0.3 ML. Figure 2 also shows the D_2 yield from the ASW/Pt interface (open circles) for a 25-ML D_2O film as a function of the H_2O spacer layer coverage deposited first on the Pt(111). This D_2 ESD yield also decays exponentially with a *1/e* constant of approximately 2.3 ±0.3 ML.
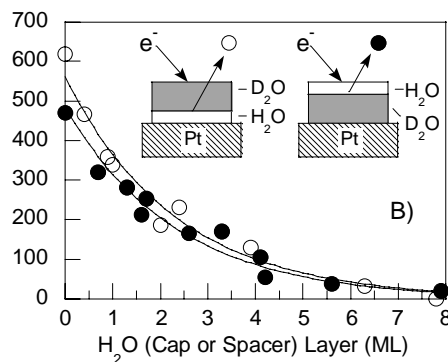

Figure 2. D_2 ESD yield vs. H_2O thickness.

These and other experiments show that 1) D_2 produced in D_2O is not trapped in ASW and can readily diffuse out at 100 K; 2) the isotope exchange reaction, $D_2 + H_2O \rightarrow HD + HDO$, is not important here; 3) one source of the D_2 is produced within the first several monolayers of the ASW film near the vacuum interface, while the rest of the D_2 originates in the ASW film within a few monolayers of the Pt substrate; and 4) the post-irradiation D_2 results from D_2 produced at the Pt/ASW interface that subsequently diffuses out of the film.

Thus, for these experiments, essentially all the electron-stimulated reactions producing D_2 occur at the inner and outer interfaces of the D_2O film. Within the sensitivity of the experiments, no D_2 is produced in the bulk of the ASW. On the other hand, the energy for the reactions is primarily absorbed in the bulk of the film and, therefore, must be transported to the interfaces over lengths of approximately 100 ML.

In the isotopic labeling experiments, very little HD is produced as would be expected if deuterium atoms or any deuterium-containing molecule produced in the bulk of the film were involved in the reactions at the interface. Therefore, it is likely that some form of electronic excitation is responsible for transporting the energy deposited in the bulk of the film to the interfaces where it reacts to form molecular hydrogen. A model invoking exciton diffusion can qualitatively explain the observations.

Reference

NG Petrik and GA Kimmel. 2003. "Electron-Stimulated Reactions at the Interfaces of Amorphous Solid Water Films Driven by Long-Range Energy Transfer from the Bulk." *Physical Review Letters* 90:116102-1661020.

Temperature-Independent Physisorption Kinetics and Adsorbate Layer Compression for Ar Adsorbed on Pt(111)

GA Kimmel,[a] M Persson,[b] Z Dohnálek,[a] and BD Kay[a]

(a)   Pacific Northwest National Laboratory, Richland, Washington
(b)   Chalmers/Göteborg University, Göteborg, Sweden

The adsorption and desorption of weakly bound (physisorbed) atoms and molecules are important fundamental gas-surface processes and, therefore, have been extensively studied. Despite its long history as a research subject, physisorption still generates significant experimental and theoretical interest. Because physisorption does not involve the transfer of electrons between the adsorbate and the substrate (no chemical bonds are formed), the lateral corrugation of the adsorbate-substrate interaction (the holding potential) is usually small. As a result, compression effects may play an important role in physisorption. Discussions of desorption kinetics are dominated by an underlying picture that is based on a lattice gas model in which the surface is composed of a fixed number of adsorption sites. Surprisingly, relatively few experimental or theoretical investigations on the effect of adlayer compression on desorption have been reported, although evidence of compression effects is found in several studies.

In this paper, we describe our study of the effects of the compressibility of an adsorbate layer on the adsorption and desorption kinetics of physisorbed atoms from surfaces with high coverages (approximately 1 ML or more). In particular, we have investigated the physisorption kinetics of Ar on Pt(111). We find that the compressibility of the Ar adlayers plays an important role in the formation of the adsorbate layer and in the desorption kinetics. We find that the first full Ar monolayer is compressed approximately 10 to 15% with respect to the uncompressed first Ar layer. We also find that compression can lead to approximately temperature-independent desorption kinetics over a temperature range of about 10 K—a range over which a desorption rate might typically be expected to vary by several orders of magnitude. Based on a quasi-equilibrium argument, we use a thermodynamic approach to calculate the chemical potential of the adsorbate layer as a function of coverage and show that this calculation semi-quantitatively reproduces the observations.

Figure 1 shows TPD spectrum for Ar adsorbed on Pt(111). Distinct peaks in the TPD spectrum that are characteristic of layer-by-layer desorption are observed. The peaks at approximately 48 K, 34 K, and 32 K correspond to desorption from the first, second, and third layers, respectively. Higher coverages resulted in multilayer desorption with a common leading edge. This TPD line shape is characteristic of physisorption for
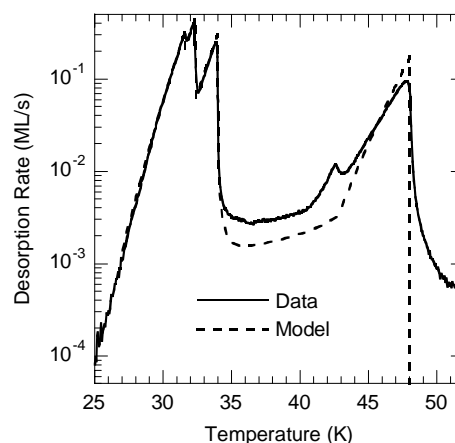

Figure 1. Ar TPD spectra from Pt(111).

many rare gases adsorbed on metal substrates. A key feature of the TPD spectrum shown in Figure 1 is the non-zero and approximately constant desorption rate observed between the first and second layer desorption peaks corresponding to desorption from the compressed monolayer. If the sample temperature is held between approximately 32 K and 42 K during deposition of the Ar, the formation of the second layer is suppressed, but the compressed monolayer is still formed (data not shown).

To gain a better understanding of desorption from the compressed adlayer, we have calculated the chemical potential as a function of coverage and temperature, $\mu_a(\theta,T)$. In this model, the chemical potential is determined from the chemical potentials of the 2D gas, the various N layer solids, and their coexistence on a flat surface. We calculate the Helmholtz free energy, $f_s(n_s,T) = \Phi_s(n_s) + f_{vib}(n_s,T)$, per atom for the monolayer, bilayer, and trilayer solids as a function of the atom surface density, n_s. The Helmholtz free energy for the adsorbate layer has contributions from the static lattice sum of the potential energy of the adsorbate layer, $\Phi_s(n_s)$, and a dynamical contribution from the lattice vibrations of the layer, $f_{vib}(n_s, T)$. $\Phi_s(n_s)$ is obtained by summing over the pair-wise interactions of the adsorbates. The adsorbates are assumed to form a simple triangular lattice for the first monolayer and the geometry of an ordered face-centered cubic crystal for more than one layer. The free energy associated with the vibrations is calculated using the quasi-harmonic approximation.

Figure 1 compares the Ar TPD spectrum calculated using the Aziz pair potential to a typical experimental TPD spectrum. In the calculation, the initial coverage and the temperature ramp rate are chosen to match the experimental conditions. At each coverage and temperature, the chemical potential is calculated from the Helmholtz free energy and the corresponding desorption rate is calculated. The new coverage and temperature are then calculated for a small time increment and the procedure is repeated. The model nicely reproduces the overall structure of the experimental TPD spectrum, including the nearly constant desorption rate observed between the peaks for the first and second layers. However, the model underestimates the desorption rate from the compressed monolayer. This research is described in more detail in Kimmel et al. (2003).

Reference

Kimmel GA, M Persson, Z Dohnalek, and BD Kay. 2003. "Temperature Independent Physisorption Kinetics and Adsorbate Layer Compression for Ar Adsorbed on Pt(111)." *Journal of Chemical Physics* 119:6776-6783.

Single-Molecule Nanosecond Anisotropy Dynamics of Tethered Protein Motions in Solution

D Hu[a] and HP Lu[a]

(a)   Pacific Northwest National Laboratory, Richland, Washington

Confined and hindered protein motions generally exist in living cells, with tethered proteins or protein domains particularly associated with and relevant to the early events of molecular interactions in cell signaling at extra- and intracellular membrane surfaces. Ensemble-averaged, time-resolved fluorescence anisotropy has been extensively applied to study the protein rotational and conformational motion dynamics under physiologically relevant conditions. However, the spatial and temporal inhomogeneities of non-synchronizable stochastic protein rotational and conformational motions are extremely difficult to characterize with such ensemble-averaged measurements (Chen et al. 2003). Here, we demonstrate the use of single-molecule nanosecond anisotropy to study the tethered protein motion of a T4 lysozyme molecule on a biologically compatible surface under water (Hu and Lu 2003). The rotational motions of tethered proteins are confined in a half-sphere whose volume is primarily defined by the linker and the surface (Figure 1).

We observe dynamic inhomogeneities of the rotational diffusion dynamics (i.e., diffusion rate fluctuation) because of interactions between the proteins and the surface. However, we also find that the long-time averages of the dynamically inhomogeneous diffusion rates of single molecules are essentially homogeneous among the single molecules examined. Moreover, tethered proteins stay predominately in solution, rather than being fixed on a modified surface. The infrequent surface interactions are not energetic enough to fix the protein rotational motions. These results suggest that the motions of proteins tethered to surfaces are dynamically in homogeneous, even if the surfaces or the local environments are homogeneous. In contrast, static inhomogeneity of the rotation dynamics can only exist when the local surface or the local environment are inhomogeneous. Furthermore, the tethered proteins are found to be in solution without rotational rate fluctuations for most of the time during the measurements,
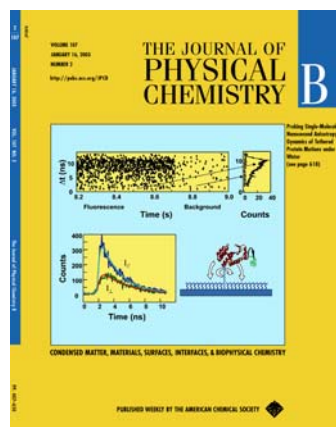

Figure 1. Illustration of a single-molecule confocal microscope with two-channel photon time-stamping time-correlated single-photon counting (TCSPC). It allows us to study the fluorescence intensity, lifetime, and anisotropy of a single molecule simultaneously by recording the arrival time and delay time of each fluorescence photon. The top-left plot is an example of the raw data of the photon time-stamping TCSPC of a detector channel. Each dot corresponds to a photon detected plotted by its arrival time (t) and delay time (Δt) [raw output from Time to Amplitude Converter in reverse timing]. The fluorescence intensity trajectory (bottom plot) is calculated from the histogram of arrival time (t) with 0.01-second time-bin resolution. The molecule was photo-bleached at 8.71 seconds. The nanosecond fluorescence decay curves (top-right plot) are the histograms of the delay time of the fluorescence photons ($t < 8.1$s) and background photons ($t > 8.1$s).

suggesting that use of tethered proteins on modified glass surfaces under water is a reasonable way to study protein dynamics in solution, as many single-molecule experiments have demonstrated. Our approach allows the recording of time trajectories of the single-molecule rotation rate fluctuation and reveals the single-molecule rotational motion over wide timescale from sub-nanoseconds to seconds (Figures 2 and 3).
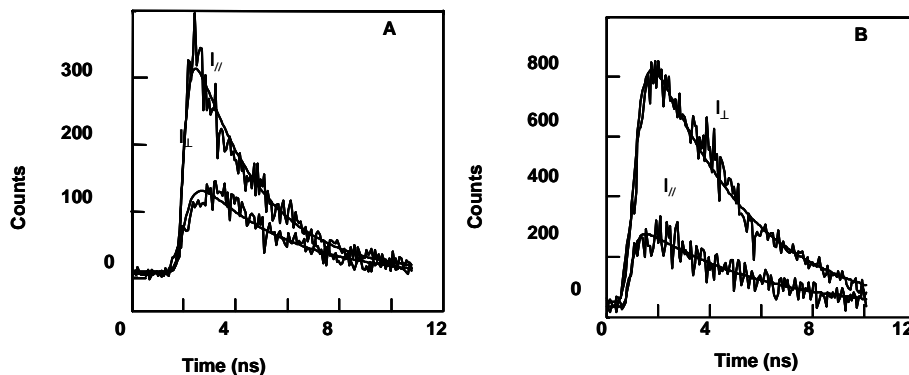

Figure 2. The parallel and perpendicular fluorescence decay and single exponential fits of a single T4 lysozyme/Alexa 488 molecule covalently linked to surface (A) and a single rhodamine 123 molecule on PMMA surface (B). The decay curves are integrated from all detected photons of parallel and perpendicular channels before photo-bleaching.
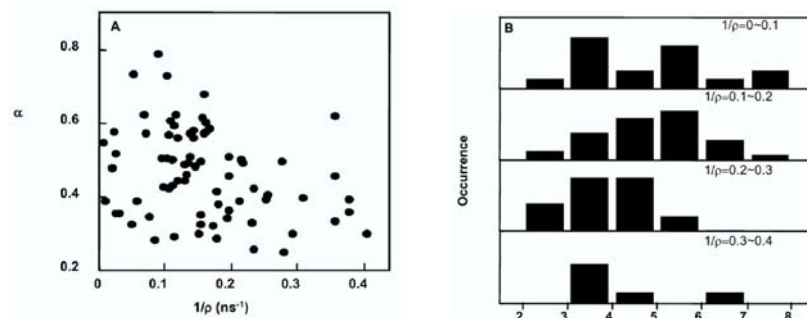

Figure 3. (A) The correlation of time-zero anisotropy (α) and anisotropy decay rate constant ($1/\rho$) from the single molecule α and $1/\rho$ trajectories. Each point corresponds to the α and $1/\rho$ values within 0.1 second bin time of the trajectory. The α and $1/\rho$ values of the full trajectories from all examined single molecules showing fluctuations are included. (B) The normalized histogram of α at different $1/\rho$ values from (A). The standard deviation of α decreases from 0.15 to 0.10 as $1/\rho$ increases from 0~0.1 to 0,3~0.4.

References

Chen Y, D Hu, ER Vorpagel, and HP Lu. 2003. "Probing Single-Molecule T4 Lysozyme Conformational Dynamics by Intramolecular Fluorescence Energy Transfer." *Journal of Physical Chemistry B* 107:7947-7956.

Hu D and HP Lu. 2003. "Single-Molecule Nanosecond Anisotropy Dynamics of Tethered Protein Motions." *Journal of Physical Chemistry B* 107:618-626.

Single-Molecule Fluorescence Imaging of Receptor Dynamics in Real Time and in Living Cells

G Orr,[a] S Ozcelik,[a] D Hu,[a] H Resat,[a] C Chen,[a] L Opresko,[a] S Wiley,[a] and S Colson[a]

(a)   Pacific Northwest National Laboratory, Richland, Washington

The work described below is aimed at elucidating the molecular interactions that govern cell fate by focusing on real-time cellular behavior of individual receptors at the cell membrane and by using and developing cutting-edge imaging technologies.

Cell membrane receptors, such as growth factor receptors, convey extracellular information to the intracellular environment that, in turn, determines the fate of the cell. The function of the receptors is tightly controlled by their molecular interactions and their spatial and temporal distribution at the cell membrane. The study of receptor interactions and dynamics in living cells and in real time has been hindered by the limitations of conventional microscopy. We have developed and perfected single-molecule fluorescence imaging techniques that enable us to identify the dynamic behavior of individual receptors and their motion patterns within membrane microstructures, and to detect subtle changes in the molecular interactions of individual receptors using fluorescence resonance energy transfer (FRET) at the level of single pairs. Our work focuses on the behavior of the epidermal growth factor receptor (EGFR) family members that control cell growth, proliferation, and migration. The four members of this family initiate molecular cascades with specific spatio-temporal properties that originate from the dynamic interactions of the receptors among themselves, with their ligands, and with other molecules in the pathway. Of particular importance are the interactions of EGFR with human epidermal growth factor 2 (HER2), a member of the family that has been implicated in certain cancers when overexpressed. We therefore have been looking at the behavior of EGFR and HER2 in the cell membrane and at the interactions between EGFR and HER2 in a series of human mammary epithelial (HME) cell lines engineered to express varying degrees of HER2.

Using high-sensitivity/high-resolution laser microscopy and relying on a series of control experiments to identify the expected photons emitted by a single fluorophore (Figure 1), as well as on other single-molecule fluorescence signatures, individual fluorescence-tagged receptors were detected as they entered membrane areas that were previously photo-bleached. By fitting a two-dimensional Gaussian curve to the fluorescent hot-spots using iterations of least-squares estimators, it was possible to follow the peak of the fitted curve and determine the motion of the spots at approximately 50-nm resolution.
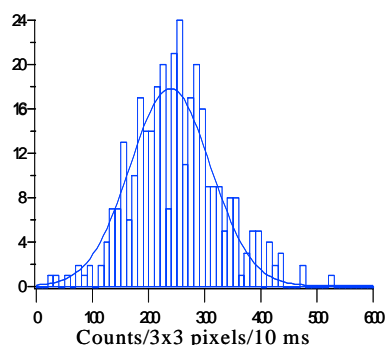

Figure 1. The expected number of photons that a single Alexa-647 molecule emits under our specific experimental conditions is 240 ±68 counts per 3x3 pixels during 10-ms laser exposure, as determined by imaging 330 single dye molecules spin-coated on glass-slides at picomolar concentrations.

This approach enabled us to identify rapidly diffusing individual receptors and their motion patterns within membrane microstructures.

The lateral diffusion of individual EGFR molecules and their dimerization partner, HER2, was tracked in HME cells, as well as in cells expressing high levels of HER2 molecules. From the mean square displacement of individual receptors, we qualified the diffusion coefficient of EGFR and HER2. The diffusion pattern of individual receptors was restricted, suggesting that the dimerization process is affected by membrane micro-domains (Figure 2). This information provides new insight into the functional significance of membrane micro-structures in receptor interactions. It was also found that the receptor ligand, EGF, modulated the diffusion of the receptors, adding to our understanding of the mechanism underlying ligand-induced receptor down-regulation.
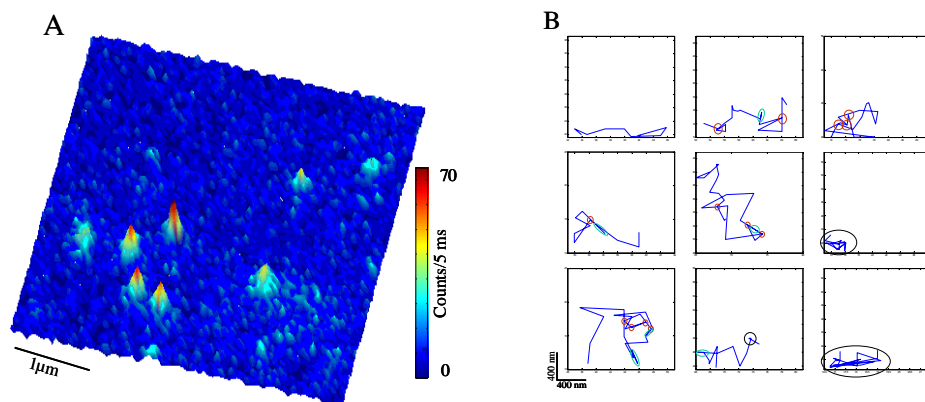

Figure 2. The pattern and rate of the lateral diffusion of individual EGFR and HER2 molecules is investigated in human mammary epithelial cells to gain an understanding of the functional significance of membrane microstructures in receptor interactions and the effect of ligand binding on receptor motion. A: Individual receptors are observed while diffusing into the field of view that was previously photo-bleached. B: From traces of individual molecules, we found that the lateral diffusion pattern of individual receptors is guided and restricted, raising the possibility that the dimerization process is affected by membrane micro-domains.

The molecular interactions between individual receptors were investigated using FRET. While toggling between two lasers, the emissions of the donor and the acceptor molecules are simultaneously acquired on two regions of interest on the charge coupled device (CCD) chip (Figure 3). This setup enables the precise detection and quantification of FRET occurrence at the level of single or few pairs, reporting subtle changes in receptor dimerization and receptor-ligand interactions. Using FRET between fluorescence-tagged receptors, we identified the molecular interactions between EGFR and HER2 under different HER2 expression levels and in response to EGF. We found a significant level of pre-formed EGFR homo-associations and EGFR-HER2 hetero-associations in HME cells as well as in cells expressing high levels of HER2, supporting an emerging picture in which ligand binding leads to a conformational rearrangement of preexisting associations.
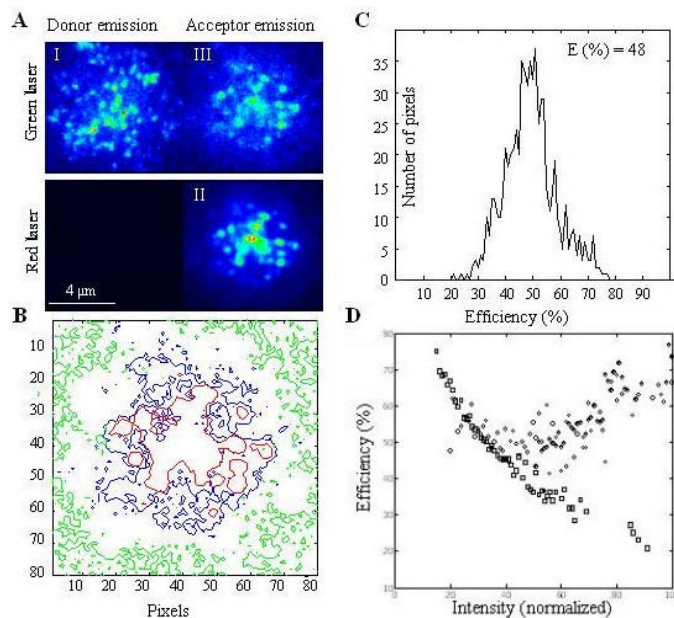
Figure 3. A: Donor and acceptor emissions are sent simultaneously to two areas on the CCD camera. The green laser directly excites the donor (A-I), and the red laser directly excites the acceptor (A-II). FRET occurrence is detected by the emission of the acceptor with donor excitation (A-III). B: Contour maps are generated from each of the three channels (A-I, -II, and -III) and are superimposed. Signals that overlap in the acceptor (A-II) and FRET (A-III) channels are further analyzed. C: FRET efficiency is calculated for each overlapping pixel (0.1 μm^2/pixel), and a histogram of FRET efficiencies is generated. The weighted average of the distribution is designated as the average FRET efficiency (E) for that membrane area. D: The anti-correlation between donor intensity (open squares), and acceptor intensity in the FRET channel (filled circles) demonstrates the transfer of energy.

Time-Lapse, Single-Molecule Fluorescence Imaging Identifies Corralled Diffusion of NMDA Receptor

G Orr,[a] D Hu,[a] S Ozcelik,[a] S Vicini,[b] and SD Colson[a]

(a)   Pacific Northwest National Laboratory, Richland, Washington
(b)   Georgetown University, Washington, D.C.

The N-methyl-D-aspartate (NMDA) receptor, a ligand-gated ion channel, plays an important role in synaptogenesis and synaptic plasticity. It has been suggested that NMDA receptors diffuse from extrasynaptic to synaptic sites, where they are trapped by anchoring proteins in a dynamic process that supports the rapid changes within the postsynaptic membrane. It is unclear, however, how fast an NMDA receptor can diffuse in the plane of the membrane, and whether the membrane microstructure plays a role in receptor insertion and escape from synaptic sites. To test the idea that NMDA receptors diffuse rapidly in the lateral dimension and explore the possibility that membrane micro-domains govern the receptor kinetic behavior in the membrane, fluorescent receptors are expressed in heterologous cells, and the motions of individual receptors are tracked using time-lapse, single-molecule fluorescence imaging. Cholesterol content is manipulated to determine its contribution to receptor dynamics and to explore the possibility that lipid rafts govern the lateral diffusion of the NMDA receptor.

In summary, we show that individual NMDA receptors are highly mobile in the plane of the membrane, and the pattern of their diffusion suggests their confinement to membrane micro-domains. Enrichment of the membrane with cholesterol, one of the main constituents of lipid rafts, seems to extend the boundaries of the confinement, and cholesterol depletion dramatically decreases receptor mobility (Figures 1 and 2). Capping the plus end of F-actin using cytochalasin D leads to the confinement of the receptor to smaller domains. These observations support the idea that lateral diffusion of NMDA receptors contributes to the rapid changes within the postsynaptic site and suggest the involvement of lipid rafts and F-actin dynamics in determining corral size for receptor diffusion.
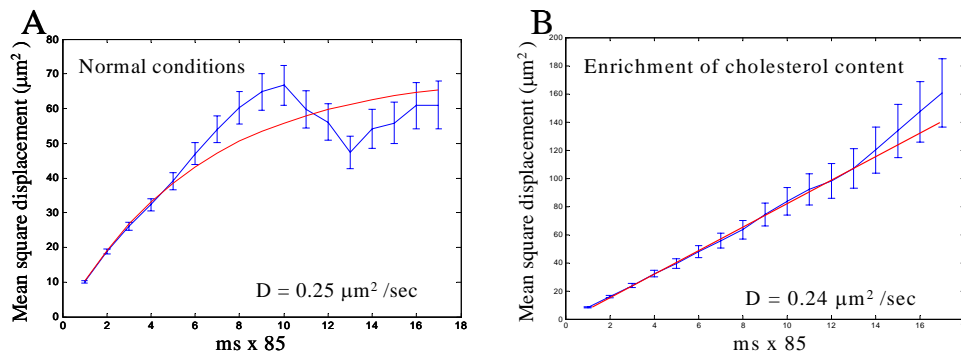

Figure 1. Manipulating the content of cell-membrane cholesterol affects the pattern but not the rate of NMDA receptor lateral diffusion. A: The non-linear relationship between mean square displacement and time indicates a confined motion under normal conditions. B: Enrichment of membrane cholesterol extends the confinement beyond the timeframe of our experiment, which is limited by the photobleaching of the individual molecules. The rate of the diffusion however is not changed by cholesterol enrichment.
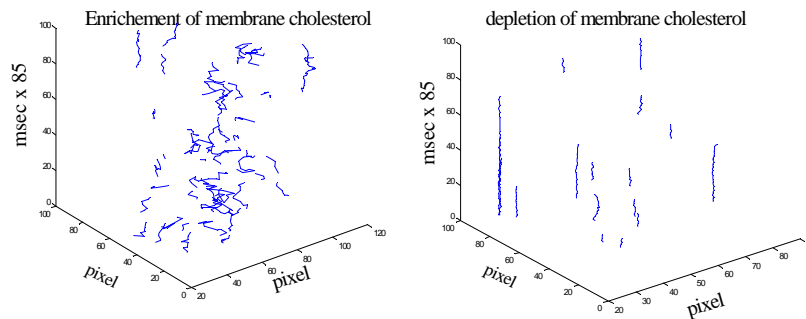
Figure 2. Traces of individual fluorescent receptors plotted over time (Z axis) show that depletion of cholesterol leads to a complete confinement of the molecules.

Radiation-Induced Genomic Instability and Non-Targeted Bystander Effects Induced by the Electron Microbeam

M Sowa Resat[a] and WF Morgan[b]

(a)   W.R. Wiley Environmental Molecular Sciences Laboratory, Richland, Washington
(b)   University of Maryland, School of Medicine, Baltimore, Maryland

Ionizing radiation induces many forms of DNA damage, both directly by energy absorption and indirectly by producing highly reactive free radicals. In recent years, it has become evident that radiation also induces delayed genomic instability, defined as an increased rate of genetic alterations in the genome of progeny of irradiated cells multiple generations after the initial insult. Delayed effects include chromosomal rearrangements and aberrations (chromosomal instability), micronuclei, gene mutations, microsatellite instability, changes in ploidy, and decreased plating efficiency. Many of these effects appear to be mediated by non-targeted effects occurring in cells that were not traversed by an ionizing particle.

Investigating potentially rare events occurring in cells that have survived exposure to ionizing radiation, as would be expected after very low doses (<10cGy), demands an assay technique that can rapidly and reliably screen very large numbers of cells. We have developed such an assay that uses a green fluorescence protein (GFP)-based homologous recombination (HR) substrate. A plasmid vector, pCMV-EGFP2Xho, that carries two GFP direct repeats is linked to an SV40 promoter-driven *neo* gene. One copy of GFP, driven by a CMV promoter, was inactivated by a +5 frame-shift mutation that created an *Xho*I site; the second copy had a wild-type coding sequence but lacked a promoter (Figure 1). This plasmid was transfected into human RKO cells (p53$^{+/+}$).
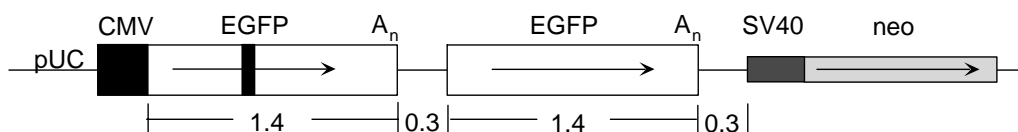

Figure 1. The plasmid vector pCMV-EGFP2Xho.

One transfected human RKO clone, RKO36, was selected for further analysis. Clone RKO36 is composed of a mixture of GFP$^+$ and GFP$^-$ cells, with those cells that were GFP$^-$ and that remained GFP$^-$ producing a uniform GFP$^-$ colony. GFP$^-$ cells can be converted to GFP$^+$ directly by radiation-induced HR, in which case all cells within a colony would be GFP$^+$. Similarly, pre-existing GFP$^+$ cells, if unchanged, will produce a GFP$^+$ colony, or they can be converted to GFP$^-$ by a variety of processes, including point mutagenesis, or induction of small- or large-scale deletions. These uniform GFP$^+$ or GFP$^-$ colonies reflect a stable GFP substrate. However, if radiation induces delayed instability at the GFP substrate, this will be reflected as mixed GFP$^{+/-}$ colonies. Such colonies can arise by delayed HR (GFP$^-$ → GFP$^{+/-}$) or delayed mutation/deletion (GFP$^+$ → GFP$^{+/-}$). Thus induced instability can be assayed in the progeny of single cells clonally expanded following exposure to a DNA

damaging agent by analyzing the induction of mixed GFP+/colonies as a function of time after exposure (Figure 2).

Our preliminary data indicate that after acute exposure to x-rays up to 10% of cells cultured after a 0.01 to 10 Gy dose produce colonies with a small number of GFP+ cells in a background of GFP- cells or a small number of GFP- cells in a background of GFP+ cells, which is indicative of delayed HR or mutation/deletion. Delayed HR

Figure 2. Schematic for radiation induced genomic instability as measured by the induction of mixed GFP+/- colonies.

was induced at low doses of ionizing radiation (< 10cGy), indicating that it is a sensitive measure of low-dose radiation effects. However, delayed HR did not show a typical dose response relationship. Consistent with prior studies, delayed chromosomal instability was induced in RKO-derived cells by relatively high doses and correlated with delayed reproductive cell death. In contrast, cells displaying delayed HR showed no evidence of delayed reproductive cell death, and there was no correlation between delayed chromosomal instability and delayed HR, indicating that these forms of genome instability arise by distinct mechanisms. Because delayed HR is induced at low doses of ionizing radiation that are not associated with reduced cell viability, it may have significant implication for assessment of radiation risk and understanding the mechanisms of radiation carcinogenesis.

The use of microbeams in radiation biology is recognized as a powerful technique for understanding the interaction of ionizing radiation with cells and tissues. In particular, this ability of a microbeam to deliver particles to a selected cell or subset of cells makes these devices valuable for investigating radiation-induced bystander effects. Much of the radioactive waste associated with the production of nuclear weapons now stored at various facilities around the world produces low linear-energy-transfer (LET) radiation typical of γ-ray emitters. At Pacific Northwest National Laboratory (PNNL), we have designed and constructed a low-cost, variable energy, low-LET electron microbeam that uses energetic electrons to mimic radiation damage produced from γ- and x-rays. The microbeam can access lower regions of the LET spectra, analogous to that produced by a ^{60}Co source.

We now propose to use this GFP-based assay to investigate potential non-targeted, bystander-like effects as well as low-dose irradiation with the electron microbeam located at PNNL. We will compare induced instability as measured with the GFP reporter construct with our well-established baseline data for instability observed cytogenetically.
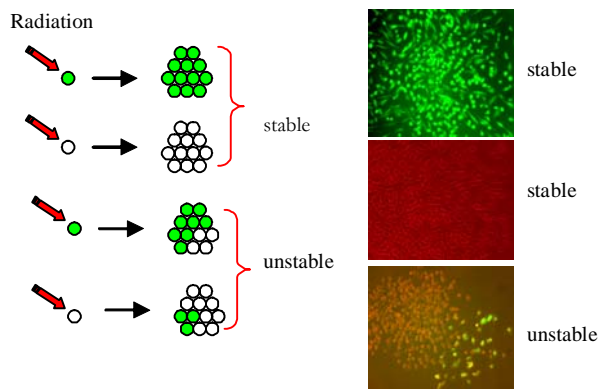
Anhydrous Nitric Acid Integrated Absorption Cross Sections: 820 to 5300 cm^{-1}

TA Blake,[a] SW Sharpe,[b] and C Chackerian, Jr.[c]

(a)   W.R. Wiley Environmental Molecular Sciences Laboratory, Richland, Washington
(b)   Pacific Northwest National Laboratory, Richland, Washington
(c)   NASA Ames Research Center and SETI Institute, Moffett Field, California

Nitric acid plays a critical role in a number of physical-chemical processes that affect the "health" of the atmosphere (Finlayson-Pitts and Pitts 2000). In the troposphere, gaseous HNO_3 dissolves in water to form a component of acid rain; in the lower stratosphere, HNO_3 condenses with water to form polar stratospheric clouds (Fahey et al. 2001); and throughout the atmosphere, gaseous HNO_3 along with peroxyacetyl nitrate (PAN) diurnally sequester the ozone-destroying NO_x species. Therefore, HNO_3 and other chemical species in the atmosphere are monitored to verify models and establish trends. Because infrared spectroscopy is used as a monitoring method and HNO_3 spectra can interfere with the spectral signatures of gaseous and aerosol species, we have determined the absorption cross section of this molecule over a wide range of frequencies.

Fourier-transform infrared absorbance measurements of small aliquots of anhydrous nitric acid were used to determine regional, integrated cross sections at 278.2 K, 298.22 K, and 323.15 K. Spectra were recorded with pressure-broadened samples (1 atmosphere nitrogen), in a 20-cm path length cell at a spectral resolution of 0.112 cm^{-1}. Spectral regions measured include the following vibrational bands: ν_1 (~3575 cm^{-1}), ν_2 (~1710 cm^{-1}), ν_3, ν_4 (~1335 cm^{-1}), and ν_5, $2\nu_9$ (~890 cm^{-1}) and regions of weaker absorption between 820 cm^{-1} and

Figure 1. Composite spectrum for 298 K obtained by fitting seven individual absorbance spectra of HNO_3 to Beers law. Each individual absorbance spectrum is taken at a different partial pressure of HNO_3.

5300 cm^{-1} (Figure 1). We observed expected changes in the distribution of ro-vibrational intensities with temperature, but to the accuracy of our measurements, cross sections integrated over entire vibrational bands are independent of temperature.
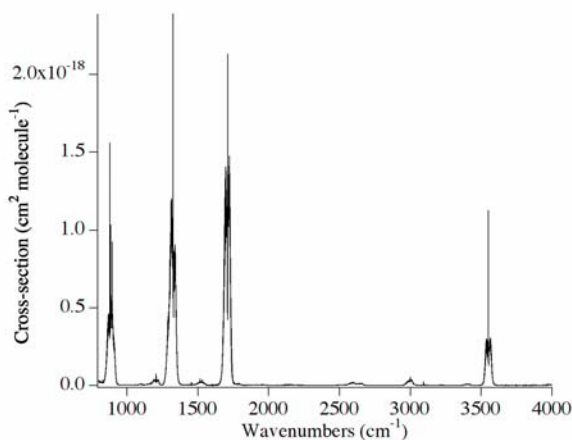
From the pressure-pathlength normalized dataset, we calculated the major integrated band intensities to be (cm/molecule) ν_5, $2\nu_9$ 2.424(65) $\times$ 10^{-17}; ν_3, ν_4 5.09(18) $\times$ 10^{-17}; ν_2, 5.71(19) $\times$ 10^{-17}, and ν_1, 1.242(32) $\times$ 10^{-17}. Our determination of the integrated absorption cross section for the ν_2 and ν_3, ν_4 regions is in excellent agreements with the data published by Giver et al. (1984), and our measurement for the ν_5, $2\nu_9$ region is about 6% lower than the value reported by those researchers. This 6% discrepancy in the long wavelength end of

the spectrum can be accounted for by the warm aperture effect found in Fourier transform spectrometers. We have eliminated this effect by placing a second aperture in the optical path of our spectrometer (Johnson et al. 2002), so we believe our value for this region is more correct. We have delivered a long-awaited confirmation of, as well as improvement on, the Giver integrated band intensities. This is important because of the 20 years the Giver results were used to scale the intensities of laboratory and atmospheric measurements to their cross section standards.

References

Fahey DW, RS Gao, KS Carslaw, J Kettleborough, PJ Popp, MJ Northway, JC Holecek, SC Ciciora, RJ McLaughlin, TL Thompson, RH Winkler, DG Baumgardner, B Gandrud, PO Wennberg, S Dhaniyala, K McKinney, TH Peter , RJ Salawitch, TP Bui, JW Elkins, CR Webster, EL Atlas, H Jost, JC Wilson, RL Herman, A Kleinbohl, and M von Konig. 2001. "The Detection of Large HNO_3-Containing Particles in the Winter Arctic Stratosphere." *Science* 291:1026-1031.

Finlayson-Pitts BJ and JN Pitts, Jr. 2000. *Chemistry of the Upper and Lower Atmosphere.* Second edition, chapters 7 and 8. Academic Press, New York.

Giver LP, FPJ Valero, D Goorvitch, and FS Bonomo. 1984. "Nitric-Acid Band Intensities and Band-Model Parameters from 610 to 1760 cm^{-1}." *Journal of the Optical Society of America B* 1:715-722.

Johnson TJ, RL Sams, TA Blake, SW Sharpe, and PM Chu. 2002. "Removing Aperture-Induced Artifacts from Fourier Transform Infrared Intensity Values." *Applied Optics* 41:2831-2839.

High-Resolution Infrared Spectroscopy and Molecular Structure of Sulfur Trioxide: The ν_3 and $2\nu_3$ Bands of $^{32}S^{16}O_3$, $^{32}S^{18}O_3$, $^{34}S^{16}O_3$, and $^{34}S^{18}O_3$

TA Blake,[a] RL Sams,[b] SW Sharpe,[b] A Maki,[c] T Masiello,[d] J Barber,[d] EtH Chrysostom,[d] N Vulpanovici,[d] JW Nibler[d] and A Weber[e]

(a) *W.R. Wiley Environmental Molecular Sciences Laboratory, Richland, Washington*
(b) *Pacific Northwest National Laboratory, Richland, Washington*
(c) *Independent Researcher*
(d) *Oregon State University, Corvallis, Oregon*
(e) *National Science Foundation and National Institute of Standards and Technology, Washington, D.C.*

Over the past several years we have been engaged in a comprehensive study of the high-resolution spectroscopy of SO_3, including all four symmetric top isotopomers formed by ^{32}S, ^{34}S, ^{16}O, and ^{18}O (Chrysostom et al. 2001; Maki et al. 2001; Barber et al. 2002; Barber et al. 2003a; Barber et al. 2003b). The initial work focused on the goal of resolving the rotational fine structure of the ν_1 Q-branch coherent anti-Stoke Raman scattering (CARS) spectrum of $^{32}S^{16}O_3$ at an instrumental resolution of 0.001 cm^{-1} (Chrysostom et al. 2001). This attempt was only partially successful, in that the K- but not the J-structure was resolved. More interesting, however, was the observed splitting of the Q-branch. This splitting was initially attributed to a Fermi resonance interaction between the ν_1 and $2\nu_4$ vibrational levels but, even with the inclusion of the somewhat more remote $2\nu_2$ level, it was found to be impossible to reproduce the details of the observed spectrum without resorting to more infrared measurements. An analysis of the high-resolution (from 0.0015 cm^{-1} to 0.0025 cm^{-1}) infrared spectrum of the hot band transitions from the ν_2 and ν_4 levels to the states $2\nu_2$ ($l = 0$), $\nu_2 + \nu_4$ ($l = \pm 1$), and $2\nu_4$ ($l = 0, \pm 2$) was found to be necessary since these levels strongly interact via Fermi resonance and indirect Coriolis interactions with the ν_1 levels. The molecular parameters that resulted from this work enabled the simulation of the ν_1 CARS spectrum with a near-perfect match with the observed one (Barber et al. 2002). In addition, the high-resolution infrared spectra of the ν_2, ν_3, ν_4, and $2\nu_3$ bands of $^{32}S^{16}O_3$ (Maki et al. 2001) have been presented and, most recently, for $^{34}S^{16}O_3$ the ν_2 and ν_4 bands have been analyzed (Barber et al. 2003a) and the interaction of combination and overtone levels of ν_2 and ν_4 with the ν_1 state has been evaluated (Barber et al. 2003b).

Our most recent results (Sharpe et al. 2003) present a systematic study of the ν_3 and $2\nu_3$ infrared bands of the four symmetric top isotopomers $^{32}S^{16}O_3$, $^{34}S^{16}O_3$, $^{32}S^{18}O_3$, and $^{34}S^{18}O_3$. The observed ν_3 and $2\nu_3$ bands are shown in Figures 1 and 2, respectively, for the four isotopomers. An internal coupling between the $l = 0$ (A_1') and $l = \pm 2$ (E') levels of the $2\nu_3$ states was observed. This small perturbation results in a level crossing between $|k{-}l| = 9$ and 12, in consequence of which the band origins of the A_1', $l = 0$ dark states could be determined to a high degree of accuracy. For example, the parent isotopic species, $^{32}S^{16}O_3$, ν_0 ($l = \pm 2$) $= 2777.87142(7)$ cm^{-1} and ν_0 ($l = 0$) $= 2766.405(17)$ cm^{-1} for the $2\nu_3$ state and ν_0 $= 1391.52025(3)$ cm^{-1} for the ν_3 state. The paper reports ground- and upper-state rotational,

centrifugal distortion, and Coriolis coupling constants for the four isotopomers. The vibrational anharmonicity constants $(\gamma^B_{33} + \gamma^{33B})$, $(\gamma^C_{33} + \gamma^{33C})$, x_{33}, and x^{33} are also reported. The spectroscopic constants for the center-of-mass substituted species $^{32}S^{16}O_3$ and $^{34}S^{16}O_3$ vary only slightly, as do the constants for the $^{32}S^{18}O_3$, $^{34}S^{18}O_3$ pair. The S-O bond lengths for the vibrational ground states of the species $^{32}S^{16}O_3$, $^{34}S^{16}O_3$, $^{32}S^{18}O_3$ and $^{34}S^{18}O_3$, are, respectively, 141.981 99(1), 141.979 38(6), 141.972 78(8), and 141.969 93(8) pm, where the uncertainties, given in parentheses, are two standard deviations and refer to the last digits of the associated quantity.
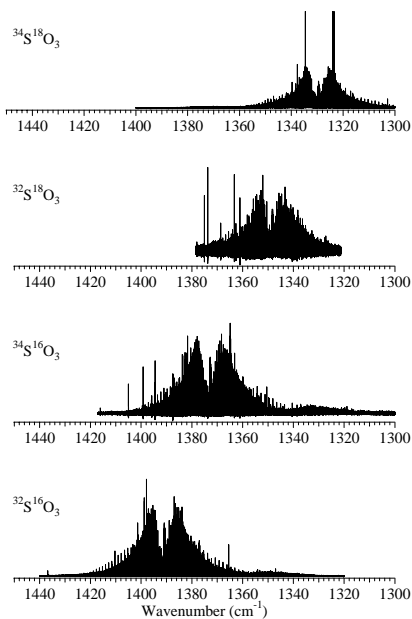

Figure 1. High-resolution infrared spectra corresponding to various ν_3 fundamental modes of the $^{34}S^{18}O_3$, $^{32}S^{18}O_3$, $^{34}S^{16}O_3$, and $^{32}S^{16}O_3$ molecules used in this detailed ro-vibrational analysis.

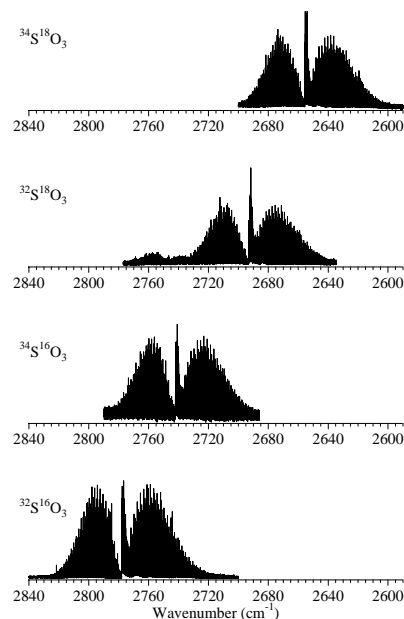**Figure 2.** High-resolution infrared spectra corresponding to various $2\nu_3$ first overtone modes of the $^{34}S^{18}O_3$, $^{32}S^{18}O_3$, $^{34}S^{16}O_3$, and $^{32}S^{16}O_3$ molecules used in this detailed ro-vibrational analysis.

Using the CARS facility at Oregon State University and the high-resolution Fourier transform infrared spectrometer in the W.R. Wiley Environmental Molecular Sciences Laboratory at PNNL, we have been able to extract extraordinary spectroscopic detail from sulfur trioxide making this the most thoroughly understood non-linear polyatomic molecule.

References

Barber J, EtH Chrysostom, T Masiello, JW Nibler, A Maki, A Weber, TA Blake, and RL Sams. 2002. "Analysis of ν_2, ν_4 Infrared Hot Bands of $^{32}S^{16}O_3$: Resolution of the Puzzle of the ν_1 CARS Spectrum." *Journal of Molecular Spectroscopy* 216:105-112.

Barber J, T Masiello, EtH Chrysostom, JW Nibler, A Maki, A Weber, TA Blake, and RL Sams. 2003a. "High Resolution Infrared Studies of the ν_2, ν_4 Bands of $^{34}S^{16}O_3$, Including Both Intensity and Wavenumber Perturbations." *Journal of Molecular Spectroscopy* 218:197-203.

Barber J, EtH Chrysostom, T Masiello, JW Nibler, A Maki, A Weber, TA Blake, and RL Sams. 2003b. "Analysis of ν_2, ν_4 Infrared Hot Bands and ν_1 CARS Spectrum of $^{34}S^{16}O_3$." *Journal of Molecular Spectroscopy* 218:204-212.

Chrysostom EtH, N Vulpanovici, T Masiello, J Barber, JW Nibler, A Weber, A Maki, and TA Blake. 2001. "Coherent Raman and Infrared Studies of Sulfur Trioxide." *Journal of Molecular Spectroscopy* 210:233-239.

Maki A, TA Blake, RL Sams, N Vulpanovici, J Barber, EtH Chrysostom, T Masiello, JW Nibler, and A Weber. 2001. "High-Resolution Infrared Spectra of the ν_2, ν_3, ν_4, and $2\nu_3$ Bands of $^{32}S^{16}O_3$." *Journal of Molecular Spectroscopy* 210:240-249.

Sharpe SW, TA Blake, RL Sams, A Maki, T Masiello, J Barber, N Vulpanovici, JW Nibler, and A Weber. 2003. "The ν_3, $2\nu_3$ Bands of $^{32}S^{16}O_3$, $^{32}S^{18}O_3$, $^{34}S^{16}O_3$, $^{34}S^{18}O_3$." *Journal of Molecular Spectroscopy* 222:142-152.

Au$_{20}$: A Tetrahedral Cluster

J Li,[a] X Li,[b,c] HJ Zhai,[b,c] and LS Wang[b,c]

(a)   *W.R. Wiley Environmental Molecular Sciences Laboratory, Richland, Washington*
(b)   *Pacific Northwest National Laboratory, Richland, Washington*
(c)   *Washington State University Tri-Cities, Richland, Washington*

Small clusters often have different physical and chemical properties than their bulk counter-parts. Materials assembled from finite-sized clusters have been intensively sought ever since the discovery of C_{60}. One of the criteria that must be met for a cluster to be used as a potential building block for cluster-assembled materials is its chemical stability relative to other reagents. A closed electron configuration with a large energy gap between the highest occupied molecular orbital (HOMO) and the lowest unoccupied molecular orbital (LUMO) is a prerequisite for the chemical stability of a cluster. Besides its high symmetry, the large HOMO-LUMO gap of C_{60} is responsible for its chemical inertness and its ability to assemble into molecular crystals.

In this paper, we describe a highly stable Au_{20} cluster discovered by combining photoelectron spectro-scopic experiments and *ab initio* calculations (Li et al. 2003). Photoelectron spectroscopy revealed that Au_{20} has an extremely large energy gap (Figure 1), even greater than that of C_{60}, and an electron affinity comparable with that of C_{60}. This observation suggests that the Au_{20} cluster should be highly stable and chemically inert. Using relativistic density functional calculations, we found that Au_{20} possesses a tetrahedral structure (inset in Figure 1), which is a fragment of the face-centered cubic lattice of bulk gold with a small structural relaxation. Au_{20} is thus a unique molecule with a similar atomic packing as the bulk, but with very different properties.

Each of the four faces of Au_{20} represents a (111) surface of fcc gold. It has a very high surface area (all the atoms are on the cluster surface), as well as a large fraction of corner sites with low coordination. The three different kinds of atoms in the T_d structure—four at the apexes, four at the center of each face, and 12 along the edges—have different coordination environments and may provide ideal surface sites to bind different molecules for catalysis (e.g., CO, O_2, and CO_2).

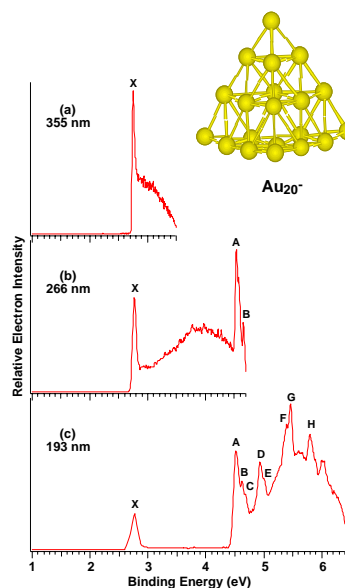**Figure 1**. Photoelectron spectra of Au_{20}^-: (a) at 355 nm (3.496 eV), (b) at 266 nm (4.661 eV), and (c) at 193 nm (6.424 eV). Note the large gap in (c) between X and A, indicating that Au_{20} is a closed shell molecule with a large HOMO-LUMO gap. The inset shows the pyramidal structure of Au_{20}.

Reference

Li J, X Li, HJ Zhai, and LS Wang. 2003 "Au$_{20}$: A Tetrahedral Cluster." *Science* 299:864-867.

All-Metal Anti-Aromatic Molecule: Rectangular Al_4^{4-} in the $Li_3Al_4^{-}$ Anion

AE Kuznetsov,[a] KA Birch,[a] AI Boldyrev,[a] X Li,[b,c] HJ Zhai,[b,c] and LS Wang[b,c]

(a) Utah State University, Logan, Utah
(b) Pacific Northwest National Laboratory, Richland, Washington
(c) Washington State University Tri-Cities, Richland, Washington

The stabilization of aromatic systems, cyclic molecules with $4n + 2$ π electrons, was first understood in organic molecules. On the basis of these ideas, numerous inorganic aromatic molecules have been synthesized and characterized, including all-metal systems (Li et al. 2001). The concept of anti-aromaticity, the corresponding destabilization seen in cyclic systems with $4n$ electrons, is perhaps best understood in cyclobutadiene. However, examples of anti-aromatic compounds outside of organic chemistry are not known.

In this paper, we describe the experimental and theoretical characterization of anti-aromaticity in $Li_3Al_4^{-}$, an all-metal system that we produced by laser vaporization and studied using photoelectron spectroscopy (Figure 1) and *ab initio* calculations (Kuznetsov et al. 2003). The most stable structure of $Li_3Al_4^{-}$ found theoretically contained a rectangular Al_4^{4-} ion stabilized by the three Li^+ ions in a capped octahedral arrangement. Molecular orbital analyses reveal that the rectangular Al_4^{4-} tetra-anion possesses $4n$ electrons, which is consistent with the $4n$ Hückel rule for anti-aromaticity.
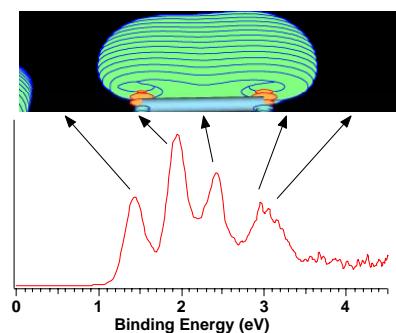
Figure 1. Photoelectron spectrum.

The discovery of anti-aromaticity in $Li_3Al_4^{-}$ completes the extension of two important chemical concepts, aromaticity and anti-aromaticity, into the realm of all-metal systems. We believe that further advancement of the aromaticity and anti-aromaticity concepts into metal territory will be valuable not only in understanding properties of metal clusters, but also in bulk metallic and alloy systems.

References

Kuznetsov AE, KA Birch, AI Boldyrev, X Li, HJ Zhai, and LS Wang. 2003. "All-Metal Antiaromatic Molecule: Rectangular Al_4^{4-} in the $Li_3Al_4^{-}$ Anion." *Science* 300:622-626.

Li X, AE Kuznetsov, HF Zhang, AI Boldyrev, and LS Wang. 2001. "Observation of All-Metal Aromatic Molecules." *Science* 291:859-861.

Probing the Intrinsic Electronic Structure of the Cubane [4Fe-4S] Cluster: Nature's Favorite Cluster for Electron Transfer and Storage

XB Wang,[(a,b)] S Niu,[(c)] X Yang,[(a,b)] SK Ibrahim,[(d)] CJ Pickett,[(d)] T Ichiye,[(c)] and LS Wang[(a,b)]

(a)   **Pacific Northwest National Laboratory, Richland, Washington**
(b)   **Washington State University Tri-Cities, Richland, Washington**
(c)   **Georgetown University, Washington, D.C.**
(d)   **John Innes Center, Norwich, United Kingdom**

The cubane [4Fe-4S] is the most common multi-nuclear metal center in nature for electron transfer and storage. Using electrospray techniques, we produced a series of gaseous doubly charged cubane-type complexes, $[Fe_4S_4L_4]^{2-}$ (L = $-SC_2H_5$, -SH, -Cl, -Br, -I) and Se-analogs $[(Fe_4Se_4L_4)]^{2-}$ (L = $-SC_2H_5$, -Cl), and probed their electronic structures with photoelectron spectroscopy (Figure 1) and density functional calculations (Wang et al. 2003). The photoelectron spectral features are similar among all seven species investigated, revealing a weak threshold feature due to the minority spins on the Fe centers and confirming the low-spin, two-layer model for the $[4Fe-4S]^{2+}$ core and its "inverted level scheme." The measured adiabatic detachment energies, which are sensitive to the terminal ligand substitution, provide the intrinsic oxidation potentials of the $[Fe_4S_4L_4]^{2-}$ complexes. The calculations revealed a simple correlation between the electron donor property of the terminal thiolate as well as the bridging sulfide with the variation of the intrinsic redox potentials. Our data provide intrinsic electronic structure information of the [4Fe-4S] cluster and the molecular basis for understanding the protein and solvent effects on the redox properties of the [4Fe-4S] active sites.

Figure 1. Photoelectron spectra of $[Fe_4S_4L_4]^{2-}$ (L = SEt, SH, Cl, Br, I) at 193 nm.

Reference

Wang XB, S Niu, X Yang, SK Ibrahim, CJ Pickett, T Ichiye, and LS Wang. 2003. "Probing the Intrinsic Electronic Structure of the Cubane [4Fe-4S] Cluster: Nature's Favorite Cluster for Electron Transfer and Storage." *Journal of the American Chemical Society* 125:14072-14081.
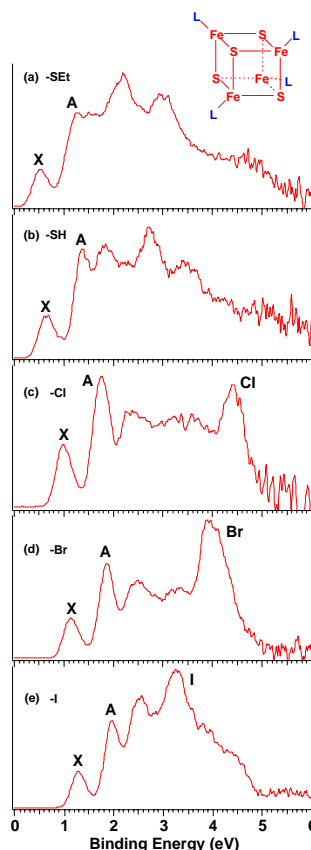
Synthesis, Characterization, and Manipulation of Helical SiO$_2$ Nanosprings

HF Zhang,[a,b] CM Wang,[a] EC Buck,[b] and LS Wang[a,b]
(a) Pacific Northwest National Laboratory, Richland, Washington
(b) Washington State University Tri-Cities, Richland, Washington

Helical nanosprings represent a new member of the family of one-dimensional nanostructures, which have attracted great attention in nanoscience recently. In addition to their anticipated structural flexibility, helical nanosprings present additional opportunities for nanoengineering, such as helicity and periodicity. Heretofore only a few helical nanostructures have been observed, and it has been challenging to devise high-yield and controlled synthesis of uniform helical nanostructures. There has been no physical characterization of the potentially novel properties of this new nanostructure.

Following our previous work on crystalline SiC/SiO$_2$ core-shell helical nanowires (Zhang et al. 2002), we have discovered amorphous silica helical nanowires. In this paper, we describe the facile synthesis of these nanosprings using a chemical vapor deposition technique and the physical characterization and manipulation using scanning and transmission electron microscopy (SEM, TEM), and atomic force microscopy (AFM). The helical silica nanosprings synthesized range from 80 to 140 nm in diameter and are several microns in length with variable periodicity (Figure 1). Stretching and contraction of these nanosprings were observed under *in situ* electron beam heating in TEM, as well as bending by an AFM tip (Zhang et al. 2003).
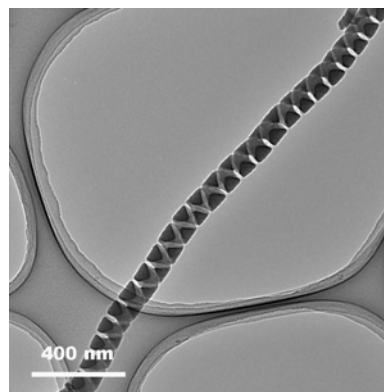
Figure 1. TEM image of a section of an amorphous SiO$_2$ helical nanospring.

Springs are important mechanical devices found in many applications. Silica glass springs in particular have been used for its low thermal expansion and contraction in comparison with that of metals. Helical silica nanosprings may have potential applications in nano-mechanical, nano-electronic, and nano-electromagnetic systems, and in composite materials.

References

Zhang HF, CM Wang, and LS Wang. 2002. "Helical Crystalline SiC/SiO$_2$ Core-Shell Nanowires." *Nano Letters* 2:941-944.

Zhang HF, CM Wang, EC Buck, and LS Wang. 2003. "Synthesis, Characterization, and Manipulation of Helical SiO$_2$ Nanosprings." *Nano Letters* 3:577-580.

User Projects

Energetic Processes: Reaction in Thin Organic Films

GB Ellison
University of Colorado, Boulder, Colorado

Theoretical Studies of Kinetic Processes in Nanoscale Ice Films

H Jonsson
University of Washington, Seattle, Washington
BD Kay, RS Smith, Z Dohnálek
Pacific Northwest National Laboratory, Richland, Washington

Laser Ablation/Ionization Characterization of Solids

JT Dickinson
Washington State University, Pullman, Washington

Probing the Electronic Structure of Metal Clusters

LS Wang
Washington State University, Tri-Cities, Richland, Washington

Near Infrared Laser Spectroscopy of Water Vapor

C Chackerian, P Pilewskie, LP Giver
NASA Ames Research Center, Moffett Field, California

Gas Phase Halogen Detection in Ambient Air

RS Disselkamp
Pacific Northwest National Laboratory, Richland, Washington

Vibration-Rotation Spectroscopy of Sulfur Trioxide

JW Nibler, N Vulpanovici
Oregon State University, Corvallis, Oregon
A Masiello
Pacific Northwest National Laboratory, Richland, Washington

Investigations of Microbial Spore Lysis Using Near-IR Laser Irradiation

DS Wunschel
Pacific Northwest National Laboratory, Richland, Washington

Aerosol Particle Generation, Collection, and Analysis

VB Mikheev
InnovaTek, Inc., Richland, Washington

Nanoparticle Fluorescence

W Chen
Nomatics, Inc., Stillwater, Oklahoma
AG Joly
Pacific Northwest National Laboratory, Richland, Washington

Laser-Induced Fluorescence Detection of C_2 and C_3 Vapor

RE Stevens
Whitworth College, Spokane, Washington

Investigation of Electronic Structure of Fe-S Clusters

LS Wang
Washington State University, Richland, Washington
S Niu
Georgetown University, Washington, Washington DC
X Wang
Pacific Northwest National Laboratory, Richland, Washington

Photoelectron Spectroscopy of Group-VI Transition Metal Oxygen Clusters

T Waters, AG Wedd, RA O'Hair
University of Melbourne, Melbourne, Victoria, Australia

An Electrochemical Investigation into the Origin of the Enhanced Reactivity of Clays in Contact with Iron Metal

BA Balko
Lewis and Clark College, Portland, Oregon
JE Amonette
Pacific Northwest National Laboratory, Richland, Washington

Measurement of the Two-Photon-Absorption Cross Section of Natural Dyes

JN Woodford
Eastern Oregon University, La Grande, Oregon

Identification of Oligoribonucleotide Products of RNA Cleavage in *Saccharomyces Cerevisiae*

D Reines
Emory University, Atlanta, Georgia

Investigation of Hydrogen Tunneling in Tropolone

RL Redington
Texas Technical University, Lubbock, Texas

Material Characterization of Fluid-Loaded Lycopodium Membrane

JB Jones-Oliveira, C Bruckner-Lea
Pacific Northwest National Laboratory, Richland, Washington
SE Barlow
W.R. Wiley Environmental Molecular Sciences Laboratory, Richland, Washington

Kinetics in Ices with Complex Compositions

RS Smith
Pacific Northwest National Laboratory, Richland, Washington
P Ayotte
Université de Sherbrooke/Concordia University (University of Sherbrooke), Sherbrooke, Quebec, Canada

Single-Particle Laboratory Studies of Heterogeneous Reactions of Trace Atmospheric Gases with Particles Present in the Troposphere

VH Grassian, BJ Krueger
University of Iowa, Iowa City, Iowa

Resonant Surface Excitation of Potassium Salts by Selective Laser Desorption

MT Perozzo
Mary Baldwin College, Staunton, Virginia

Fourier Transform Infrared Spectroscopy and Temperature Program Desorption (TPD) Studies of Amorphous Solid Water (ASW) as a Function of Dosing Temperature

JM Donev, S Fain
University of Washington, Seattle, Washington

Jet Spectrum of Nitromethane

DS Perry
University of Akron, Akron, Ohio

Measurement of Absolute Infrared Absorption Cross Sections of Nitric Acid

C Chackerian
NASA Ames Research Center, Moffett Field, California

High-Resolution Infrared Spectroscopy of Boron Trifluoride

AG Maki
Private Consultant, Mill Creek, Washington

Study of Nd^{3+} Surface Adsorption on Calcite

SH Withers-Kirby
University of Central Florida, Orlando, Florida

Cellular Responses to Ionizing Radiation as Examined by FTIR

F Severcan
Middle East Technical University, Ankara, Turkey
MB Resat, BA Holben
W.R. Wiley Environmental Molecular Sciences Laboratory, Richland, Washington

Size Resolved Chemical Composition of Automobile Generated Aerosol Via Single Particle Real-Time, Ion-Trap Mass-Spectrometry

DG Imre, A Zelenyuk
Pacific Northwest National Laboratory, Richland, Washington

Spectroscopic Infrared Properties of Hydrogen Cyanide

MD Venkataraman
College of William and Mary, Hampton, Virginia

Evaluation of Municipal Incinerator Contribution to Spokane Particulate Matter

DD Finn
Washington State University, Pullman, Washington
A Laskin
W.R. Wiley Environmental Molecular Sciences Laboratory, Richland, Washington

Scanning Mass Spectroscopy of Aerosols

GC Nieman
Monmouth College, Monmouth, Illinois

Photochemistry of a Diluted Magnetic Semiconductor Quantum Dot: A Possible Photocatalyst for Water Splitting

DR Gamelin, KR Kittilstved
University of Washington, Seattle, Washington
AG Joly
Pacific Northwest National Laboratory, Richland, Washington

High-Resolution Infrared Spectroscopy of Methyl Nitrite

LM Goss
Idaho State University, Pocatello, Idaho

Pd Nanoclusters Supported on MgO(100): Effects of Cluster Size on Chemisorption Properties

SL Tait, S Fain, CT Campbell
University of Washington, Seattle, Washington
RS Smith, Z Dohnálek
Pacific Northwest National Laboratory, Richland, Washington

Microscopic Characterization of Sampling Inlet Penetration Efficiency for DOE G-1 Research Aircraft

FJ Brechtel
Brookhaven National Laboratory, Upton, New York

Laboratory Studies of Atmospheric Processing of Sea Salt

BJ Finlayson-Pitts, JN Pitts, RC Hoffman
University of California Irvine, Irvine, California

Development of an Electrospray Photoelectron Spectroscopy Apparatus with a Low-Temperature Ion Trap

LS Wang
Washington State University, Richland, Washington

High-Resolution Matrix Assisted Laser Desorption/Ionization Imaging of Biological Samples

DS Wunschel
Pacific Northwest National Laboratory, Richland, Washington

High Resolution Infrared Spectroscopy of Isotopically Substituted Butadienes

NC Craig
Oberlin College, Oberlin, Ohio

High-Resolution Infrared Spectroscopy of Acetaldehyde

JT Hougen
National Institute of Standards and Technology, Gaithersburg, Maryland

Investigation of the Electronic Structure of Fe-S Clusters

LS Wang
Washington State University, Richland, Washington
CJ Pickett
John Innes Centre, Norwich, United Kingdom

Investigation of Zwitterions in the Gas Phase

SR Kass
University of Minnesota, Minneapolis, Minnesota
LS Wang
Washington State University, Tri-Cities, Richland, Washington

Investigation of the Electronic Structure of Fe-S Clusters

T Ichiye, LS Wang
Washington State University, Tri-Cities, Richland, Washington

Investigation of Aromatic and Other Novel Gas Phase Atomic Clusters and Molecules

AI Boldyrev, BM Elliott
Utah State University, Logan, Utah
LS Wang
Washington State University, Tri-Cities, Richland, Washington

Computational Chemistry Modeling of Main-Group and Transition-Metal Cluster Systems

LS Wang, K Boggavarapu
Washington State University, Tri-Cities, Richland, Washington
J Li
W.R. Wiley Environmental Molecular Sciences Laboratory, Richland, Washington

Absolute Infrared Absorption Cross Section of CF_3SF_5

CP Rinsland
NASA Langley Research Center, Hampton, Virginia

Single-Molecule Enzymatic Reaction Dynamics

HP Lu, D Hu
Pacific Northwest National Laboratory, Richland, Washington

Theoretical Models of the Adsorption and Desorption Dynamics in Compressed Monolayers

M Persson
Chalmers/Goteborgs University, Goteborg, Sweden
BD Kay, RS Smith, Z Dohnálek, GA Kimmel
Pacific Northwest National Laboratory, Richland, Washington

Adiabatic Following Spectroscopy Using Quantum Cascade Lasers

G Duxbury
University of Strathclyde, Glasgow, United Kingdom

Microscopic Studies of Hydration and Corrosion in Nuclear Materials Disposition

SA Joyce
Los Alamos National Laboratory, Los Alamos, New Mexico

Mexico City Municipal Area Air Pollution Study, 2003

MJ Molina, L Molina, KS Johnson, BM Zuberi
Massachusetts Institute of Technology, Cambridge, Massachusetts
ML Alexander, JP Cowin, BT Jobson, P Prazeller
Pacific Northwest National Laboratory, Richland, Washington
AB Laskin, DJ Gaspar
W.R. Wiley Environmental Molecular Sciences Laboratory, Richland, Washington

Surface-Induced Dissociation of Peptides Using FTICR Mass Spectrometry

K Kuppannan, VH Wysocki, KA Herrmann, FM Fernandez
University of Arizona, Tucson, Arizona
J Laskin, JH Futrell
Pacific Northwest National Laboratory, Richland, Washington

High-Resolution Infrared Spectroscopy of Nitrogen Dioxide and Water

MA Smith
NASA Langley Research Center, Hampton, Virginia
RL Sams
Pacific Northwest National Laboratory, Richland, Washington
TA Blake
W.R. Wiley Environmental Molecular Sciences Laboratory, Richland, Washington

High-Resolution Infrared Spectroscopy of Methane

L Brown
Jet Propulsion Laboratory, Pasadena, California
RL Sams
Pacific Northwest National Laboratory, Richland, Washington
TA Blake
W.R. Wiley Environmental Molecular Sciences Laboratory, Richland, Washington

Measure the Anisotropy of a Membrane Protein at a Cell Membrane

J Zheng
University of Washington, Seattle, Washington
HP Lu
Pacific Northwest National Laboratory, Richland, Washington

Ultrasonic Catalysis of Chemical Reactions

AM Williams
Gonzaga University, Spokane, Washington
KM Judd
Pacific Northwest National Laboratory, Richland, Washington

Electron-Induced Low-Dose Hypersensitivity

MC Joiner, B Marples
Wayne State University, Detroit, Michigan
EJ Ashjian
Southridge High School, Kennewick, Washington
MB Resat, GR Holtom, BA Holben
W.R. Wiley Environmental Molecular Sciences Laboratory, Richland, Washington

Electron-Induced Genomic Instability

MB Resat, GR Holtom, BA Holben
W.R. Wiley Environmental Molecular Sciences Laboratory, Richland, Washington
WF Morgan, A Snyder
University of Maryland, Baltimore, Maryland
EJ Ashjian
Southridge High School, Kennewick, Washington

Triplet Decay Pathways of the Electrically Conducting Polymer Poly[2-methoxy-5-(2′-ethylhexyloxy)-1,4-phenylenevinylene]

DM Laman, ZC Jacobson, SW Miller
Central Washington University, Ellensburg, Washington

Laser-Induced Neutral Metal Atom Desorption from Magnesium Oxide and Lithium Fluoride Probed via Optical Spectroscopies

CN Afonso
Instituto de Optica, Madrid, Spain

Single-Molecule Dynamics of Protein/DNA Interactions

JJ Han, AD Li
Washington State University, Pullman, Washington
HP Lu
Pacific Northwest National Laboratory, Richland, Washington

Using the Environmental Scanning Electron Microscope for Studying the Atmospheric Transformations of Organic and Inorganic Particles

Y Rudich
Weizmann Institute, Rehovot, Israel

Fluorescence Imaging of Cellular Protein Dynamics

GM Carr
Brigham Young University, Provo, Utah
G Orr, SD Colson, D Hu
Pacific Northwest National Laboratory, Richland, Washington

Dissociative Charge Inversion of Peptides by Surface-Induced Dissociation

J Alvarez, RG Cooks
Purdue University, West Lafayette, Indiana
J Laskin, AK Shukla, JH Futrell
Pacific Northwest National Laboratory, Richland, Washington

Inelastic Electron Scattering Cross Section Measurements in Liquid Water

C Brown
Wadsworth Center, Albany, New York
RG Tonkyn
Pacific Northwest National Laboratory, Richland, Washington

Dynamics Studies of Surface-Induced Dissociation of Polyatomic Ions

AK Shukla, T Rezayat
Pacific Northwest National Laboratory, Richland, Washington

Fluorescence Microscopy of Cells and Particles

GR Holtom
W.R. Wiley Environmental Molecular Sciences Laboratory, Richland, Washington
BJ Arthurs
Pacific Northwest National Laboratory, Richland, Washington

Development of Data Analysis and Visualization Software – SpectraMiner

P Imrich, K Mueller
State University of New York at Stony Brook, Stony Brook, New York

Computer Programming of Data Acquisition Board for Single Particle Laser Ablation Time-of-Flight Mass Spectrometer (SPLAT-MS)

S Jambawalikar
State University of New York at Stony Brook, Stony Brook, New York
A Zelenyuk
Pacific Northwest National Laboratory, Richland, Washington

Signal Transmissions in Three-Dimensional Cell Structures

L Opresko
Pacific Northwest National Laboratory, Richland, Washington
MB Resat, BA Holben
W.R. Wiley Environmental Molecular Sciences Laboratory, Richland, Washington

Determination of the Mo—OX Bond Strengths in Oxomolybdenum Model Complexes

P Basu, V Nemykin
Duquesne University, Pittsburgh, Pennsylvania
J Laskin
Pacific Northwest National Laboratory, Richland, Washington

Dye Studies on CHO Cells

MU Mayer-Cumblidge
Pacific Northwest National Laboratory, Richland, Washington

Ultrastructural Properties of Small Intestinal Submucosa

AD Janis, MC Hiles
Cook Biotech Incorporated, West Lafayette, Indiana

Laser-Materials Interactions: Theory and Experiment

AL Shluger, PV Sushko
University College London, London, United Kingdom

Single Particle Analysis of Smoke Aerosols During the Summer 2002: Yosemite Aerosol Characterization Study

JL Hand
Colorado State University, Fort Collins, Colorado

Second Harmonic Generation from Organic Water/Air Interfaces

AT Maccarone, GB Ellison
University of Colorado, Boulder, Colorado

Surface-Induced Dissociation of Polyatomic Ions

J Laskin, JH Futrell
Pacific Northwest National Laboratory, Richland, Washington

Single-Molecule Approach for Understanding EGFR Molecular Interactions

G Orr, HS Wiley, L Opresko, H Resat, D Hu, SD Colson, S Ozcelik

Pacific Northwest National Laboratory, Richland, Washington

Electron Stimulated Reactions in Thin Water Films

GA Kimmel, NG Petrik

Pacific Northwest National Laboratory, Richland, Washington

Condensed Phase Chemical Physics of Low-Temperature Amorphous Solids and Gas Surface Interactions

RS Smith, BD Kay, Z Dohnálek

Pacific Northwest National Laboratory, Richland, Washington

Use of Fluorimeter for Quantum Efficiency Studies on Semiconductor Quantum Dots

MG Warner, C Bruckner-Lea

Pacific Northwest National Laboratory, Richland, Washington

Single-Molecule Electron Transfer Dynamics

HP Lu, VP Biju, D Hu

Pacific Northwest National Laboratory, Richland, Washington

Site-Specific Spectroscopy and Optical Imaging

HP Lu, D Pan

Pacific Northwest National Laboratory, Richland, Washington

AFM-Enhanced FLIM and Raman Imaging

HP Lu, D Hu, D Pan, VP Biju

Pacific Northwest National Laboratory, Richland, Washington

Protein-Protein Interaction Dynamics

HP Lu, X Tan

Pacific Northwest National Laboratory, Richland, Washington

Microbial Cell Analysis and Imaging

HP Lu, VP Biju

Pacific Northwest National Laboratory, Richland, Washington

Ion Channel Protein Dynamics in Lipid Bilayer

HP Lu

Pacific Northwest National Laboratory, Richland, Washington

Staff

Wayne P. Hess, Chief Scientist, Technical Lead
(509) 376-9907, wayne.hess@pnl.gov

Jayme Crow, Administrative Secretary
(509) 376-2642, jayme.crow@pnl.gov

Stephan E. Barlow, Chief Scientist
(509) 376-9051, se.barlow@pnl.gov

Gary R. Holtom, Chief Scientist
(509) 376-5331, gary.holtom@pnl.gov

Kenneth M. Beck, Senior Research Scientist
(509) 376-9152, kenneth.beck@pnl.gov

Thomas A. Blake, Senior Research Scientist
(509) 376-8974, ta.blake@pnl.gov

John Daschbach, Senior Research Scientist
(509) 376-2467, john.daschbach@pnl.gov

Martin J. Iedema, Senior Research Scientist
(509) 376-6039, martin.iedema@pnl.gov

Alex Laskin, Senior Research Scientist
(509) 376-8741, alexander.laskin@pnl.gov

Marianne Sowa Resat, Senior Research Scientist
(509) 376-9104, marianne.sowa-resat@pnl.gov

Matrixed Staff

Alan G. Joly, Senior Research Scientist
(509) 376-7707, agjoly@pnl.gov